

Comprehensive Model for Charge Carrier Recombination in Czochralski-Grown Silicon Due to Oxygen Precipitation in Industrial Solar Cell Manufacturing

Stephan Maus,* Sebastian Mack, Jonas Schön, Marius Meßmer, Andreas Wolf, and Oliver Paul

Oxygen precipitates are among the most detrimental oxygen-related silicon bulk defects formed during solar cell manufacturing. These defects are formed only during high-temperature processes, impeding an identification of prone materials during incoming inspection. Moreover, the prediction of oxygen-precipitate-related bulk charge carrier recombination currently requires advanced numerical simulation. This work presents an easily implementable model to predict the bulk carrier lifetime limit, using the temperature–time profile of a high-temperature process as well as the material properties as the input data. In addition to published analytical descriptions of oxygen precipitation, an empirical description of the retarded growth of small precipitates is included. Furthermore, the time-lag in nucleation is explicitly considered, which is, to our knowledge, not implemented in oxygen precipitation modeling so far. The calibration of the two free parameters of the model is achieved using the experimental data of 19 different thermal process combinations performed using a single material. This results in a good agreement not only for the material used for calibration but also for other silicon materials. A validation based on passivated emitter and rear cells as well as on test structures confirms the ability of the model to predict bulk carrier lifetimes after solar cell processing.

1. Introduction

Oxygen precipitates (OPs) are common defects in Czochralski-grown silicon (Cz-Si) and are known to enhance carrier recombination in bulk silicon.^[1] These defects form, e.g., during high-temperature (HT) processes in solar cell manufacturing and hence are hard to identify during incoming inspection.^[2] For both p- and n-type silicon solar cell concepts, the enhanced recombination was reported to cause severe efficiency degradation. For p-type passivated emitter and rear cells (PERCs) and n-type passivated emitter rear totally diffused (PERT) cells, efficiency degradations of 5%_{abs}^[1] and 1.5%_{abs}^[3] were reported, respectively. These efficiency degradations are based on a decrease in both short-circuit current density j_{SC} and open-circuit voltage V_{OC} . Although technological progress has continuously reduced the concentration of interstitial oxygen in Cz-Si ingots,^[4,5] the recombination in the bulk becomes more and more relevant

due to the ongoing development in solar cell research to minimize surface recombination. In addition, new technologies such as the tunnel oxide passivating contact (TOPCon)^[6–8] cell concept enter the market, whose manufacturing requires a higher thermal budget compared to the currently dominant PERC technology.^[6,9] The premise of this work is that a detailed investigation as well as a numerical or analytical description of OP evolution during the HT process steps can enable a prediction of the OP impact on cell performance. Such understanding enables to reduce process development costs and can ensure process stability with respect to material property variations, leading to more sustainable and economic solar cell manufacturing.

OPs constitute a well-known topic in microelectronics especially in the integrated circuit (IC) industry.^[10–13] As metallic impurities in the near-surface region significantly degrade IC device performance^[14,15] and even result in shorted devices,^[10] impurity gettering has become common practice. For this purpose, the impurity gettering property of OPs is taken advantage of and HT processes are optimized to form OPs effectively.^[10,13] However, these processes are performed at constant temperatures with durations up to several tens of hours. Typical HT

S. Maus, S. Mack, J. Schön, M. Meßmer, A. Wolf
Department of Photovoltaic Production Technology
Fraunhofer Institute for Solar Energy Systems (ISE)
Heidenhofstrasse 2, 79110 Freiburg, Germany
E-mail: stephan.maus@ise.fraunhofer.de

J. Schön
Department of Sustainable Systems Engineering (INATECH)
University of Freiburg
Emmy-Noether-Straße 2, 79110 Freiburg, Germany

O. Paul
Department of Microsystems Engineering (IMTEK)
University of Freiburg
Georges-Köhler-Allee 103, 79110 Freiburg, Germany

 The ORCID identification number(s) for the author(s) of this article can be found under <https://doi.org/10.1002/solr.202200980>.

© 2022 The Authors. Solar RRL published by Wiley-VCH GmbH. This is an open access article under the terms of the Creative Commons Attribution-NonCommercial-NoDerivs License, which permits use and distribution in any medium, provided the original work is properly cited, the use is non-commercial and no modifications or adaptations are made.

DOI: [10.1002/solr.202200980](https://doi.org/10.1002/solr.202200980)

processes for solar cell manufacturing consist of varying temperatures with durations of only a few hours. Therefore, the described findings and analytical models developed based on HT processes for IC production need to be adapted to describe the formation of OPs during HT process steps in solar cell manufacturing.

According to current understanding, precipitate nuclei in the form of aggregates of a few O atoms are formed during pulling of a Cz-Si ingot and, therefore, already exist in as-cut silicon wafers.^[16,17] The requirements for nucleation are a sufficient oxygen concentration, the existence of lattice defects, especially vacancies acting as nucleation sites, and a specific thermal history of the material, providing the energy to form the nuclei.^[16–18] The first two conditions are fulfilled along most of the Cz-Si ingots. Due to the reaction between the silicon melt and the crucible, the crystallized silicon is saturated with interstitial oxygen (O_i).^[16] Furthermore, the majority of ingots are pulled in vacancy mode in order to achieve a high throughput.^[3] The nucleation takes place in the temperature range from 400 to 850 °C with two maxima in the nucleation rate at about 750 °C and about 500 °C, whereby the size and density of nuclei increase with duration.^[13,16,17] To achieve a sufficient diameter of a Cz-Si ingot, the pulling speed is reduced at the beginning, leading to an extended duration in the nucleation temperature range and therefore to a high concentration of nuclei near the seed end.^[3,19] Korsós et al.^[3] found small bulk microdefects (BMDs) after the ingot cool-down, which grew during subsequent HT processing. These authors interpreted the BMDs present after ingot cool-down to be nuclei for oxygen precipitation. The investigated 750 mm-long ingot was pulled with a relatively slow speed of 36 mm h⁻¹, leading to a cooling rate of about 100 K h⁻¹ at temperatures above 1300 °C.^[20] However, in current Cz-Si manufacturing (especially for photovoltaics) the pulling rate is much higher ($\geq 60 \text{ mm h}^{-1}$),^[18,21] leading to high cooling rates ($\gg 100 \text{ K h}^{-1}$) at high temperatures where the temperature–time profile flattens out as room temperature is approached.^[20,21] Nielsen et al.^[5] recently even introduced active cooling near the melt/crystal interface in industrial ingot manufacturing to increase throughput. A higher cooling rate may play a significant role for avoiding precipitate nucleation during ingot cool-down.

Based on classical nucleation theory, only the maximum in the nucleation rate near 750 °C is expected,^[17] where the origin of the second maximum at about 500 °C is still a matter of debate. Newman proposed the second maximum to be related to a change from macroscopic to microscopic kinetics as the temperature is lowered.^[17] Alternatively, Inoue et al. argued that the second maximum is due to the generation of thermal donors (TDs) in the temperature range between 350 and 500 °C.^[22] These TDs are suggested to act as nucleation sites for OPs or embryos for homogeneous nucleation,^[22] which are also recombination active.^[2,3,23] TDs are known to be aggregates of a few O_i atoms, whose density (number per volume) increases with duration within the generation temperature range, similar to OP nuclei.^[16,17] Recently, Olsen et al. found an inverse correlation of TD density with pulling rate during Cz manufacturing,^[24] which can be attributed to a change in duration within the generation temperature range. Furthermore, TDs act as double donors and therefore influence the resistivity of the wafers below 500 °C.^[16] Above 500 °C, TDs lose their electrical^[16] and recombination activity.^[2,3,23] The change in electrical activity, and hence resistivity, allows to calculate their

density C_{TD}.^[25–27] This relation between TDs in the as-cut state and the susceptibility of the material to form OPs in subsequent HT process steps has been reported,^[3,19] supporting Inoue et al.'s argument.^[22] Typically, the concentration of TDs decreases from seed to tail of an ingot, while C_{TD} = $3 \times 10^{14} \text{ cm}^{-3}$ was found to be the threshold for susceptible material.^[3]

Another impact on oxygen precipitation is the gas atmosphere during the HT processes, which is known to influence the nucleation rate.^[16,18,28] During oxidation, silicon self-interstitials are emitted into the bulk, reducing the number of vacancies and thus nucleation sites. Therefore, in inert gas atmosphere (e.g., nitrogen) nucleation is found to be enhanced in comparison with an oxidizing ambient.

The temperature-dependent growth of nuclei into large precipitates is a well-studied topic.^[13,16,17,29] Thereby, precipitates grow or dissolve depending on their size and the process temperature, more precisely on their radius *r* with respect to the critical radius *r_c*, which increases with temperature. Precipitates with a radius smaller than *r_c* dissolve, while those with a larger radius grow. This results in a temperature-dependent density and size distribution of precipitates.

One opportunity for the beneficial usage of the temperature-dependent dissolution of nuclei or small precipitates is the so-called Tabula Rasa (TR) treatment.^[10,13,29,30] This treatment is a first process to condition wafers before any subsequent thermal treatment. During the TR treatment, the temperature is rapidly increased to reach a plateau above 1000 °C, whereupon it is rapidly ($\gg 100 \text{ K h}^{-1}$) decreased to reach the unloading temperature. In IC industry, a several-hours-long TR treatment is used to dissolve nuclei, possibly formed during ingot cool-down, and to facilitate outdiffusion of interstitial oxygen near the surface. Subsequently, a nucleation process near 700 °C enables the controlled formation of the desired density of nuclei followed by an intermediate process at about 800 °C to grow the OPs large enough to survive the subsequent temperature ramp up toward the actual growth step at about 1000 °C.^[10,13] Hence, the sequence of TR, nucleation, and growth step limits the growth of OPs to the wafer bulk and omits OP formation near the surface, where it might degrade IC devices.^[10] Nevertheless, a challenge related to the TR is the so-called time-lag in nucleation. Inoue et al. reported that after a HT treatment (reported for temperatures $\geq 900 \text{ °C}$) followed by a rapid cool-down ($> 100 \text{ K h}^{-1}$, reported for a minimum decrease of 100 K) the nucleation was inhibited for several tens of hours,^[22] whereby an extended nucleation (typically at about 750 °C) was necessary to overcome the time-lag. These authors described the possibility to shorten the time-lag in nucleation by adding a treatment at about 450 °C for a duration of a few hours before the actual nucleation process.^[22] Thereby, the ability for nucleation was recovered, which might be related to the generation of TDs in this temperature range, as discussed above.

The difficulty of the time-lag in nucleation for the IC industry is actually a benefit for photovoltaics. Indeed, after wafers have been conditioned by a TR process, an immediate nucleation due to subsequent thermal processes is avoided. Hence, no detrimental OPs are formed. This holds as long as no thermal process is performed at about 450 °C for a few hours nor at about 750 °C for an extended duration ($> 10 \text{ h}$), which are both uncommon processes for photovoltaic (PV) applications. For this reason, TR treatments were

introduced in PV research in earlier work^[29,30] but have not been adapted in the PV industry so far because of additional costs.

The growth of large OPs ($r \gg r_c$) is limited by the diffusion of O_i toward the precipitates.^[16,17] During growth, a morphological transformation of the OPs takes place, which proceeds at a given rate within a population of growing precipitates and does not depend on the size of the OPs but on their density, the concentration of interstitial oxygen C₀, and the growth temperature.^[31] The mechanism is not fully understood yet.^[31] After the transformation, the OPs are strained and thus become visible after preferential etching.^[16,18,32] According to Murphy et al., OPs then act as strong recombination centers, whereas the recombination at unstrained precipitates is weak.^[33] The recombination activity of OPs scales with the surface area of strained precipitates.^[16,34] Under low injection conditions ($\ll 10^{15} \text{ cm}^{-3}$), the bulk carrier lifetime limitation is at a lower level in p-type than in n-type silicon, while at high injection ($> 10^{15} \text{ cm}^{-3}$) the lifetime limitations converge.^[34] A detrimental impact on the recombination activity of OPs is due to metallic impurities, which are gettered at the OPs, thereby enhancing the effective defect density at the same trap levels associated with OPs.^[35]

The vacancy-mode Cz-pulling results in a radial vacancy gradient with decreasing vacancy concentration toward the wafer edge, leading to less OP formation in that direction.^[36] Furthermore, small temperature deviations can occur in the melt and at the crystal growth interface due to variations in thermal convection, crystal rotation during pulling, and crystal pull rate, leading to microscopic growth rate fluctuations.^[36] As a result, impurities including oxygen are inhomogeneously incorporated into the growing ingot, leading to radial interstitial oxygen striations.^[16] The OP precipitation proceeds primarily in regions of high interstitial oxygen, leading to OPs within these striations.^[36,37] Due to a spatial resolution in the 10–100 μm range and a relatively low injection level during photoluminescence (PL) measurements, a significant image smearing due to the lateral diffusion of carriers is observed, extending over several tens of micrometers.^[36] The resulting cumulative effect of OPs leads to the typical circular defect pattern in PL measurements,^[2,38] as exemplarily shown in Figure 1.

This work presents a comprehensive model to approximate the bulk carrier lifetime limit due to OP formation using Shockley–Read–Hall (SRH) statistics, based on material properties and temperature–time profiles of HT processes applied during solar cell manufacturing. In addition to published analytical descriptions of oxygen precipitation, an empirical description of the retarded growth of small precipitates is included. Furthermore, the time-lag in nucleation is explicitly considered, which was, to our knowledge, not implemented in OP modeling so far. In contrast with published numerical simulations^[39,40] and own previous work,^[41] this model is easily implemented without recurring to specialized numerical simulation tools.

Section 2 presents the model details for the prediction of the OP-related silicon bulk carrier lifetime limit. In Section 3, the experiments for calibration and validation of the model are described, while Section 4 presents their results. Furthermore, Section 4 reports a comparison of the model with our previous simulation.^[41] The results as well as remaining open questions are discussed in Section 5, whereupon Section 6 summarizes and concludes this work.

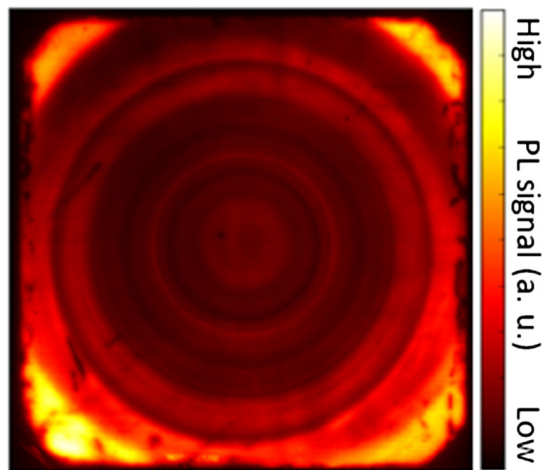


Figure 1. Photoluminescence image of a passivated Cz-Si wafer with an edge length of 156 mm after a HT treatment, showing circular defect pattern of low carrier lifetime regions due to oxygen precipitation.

2. Modeling

As a first step toward a model of oxygen precipitation, the starting “as-cut” condition of the wafer must be defined. We assume an ingot cooling rate larger than 100 K h^{-1} at high temperatures and therefore a time-lag in nucleation. The time-lag is overcome as the ingot cool-down temperature–time profile flattens out at low temperatures, leading to TD generation depending on the concentration of interstitial oxygen, C₀, and on the duration near 450 °C. These TDs act as nucleation sites or embryos for homogeneous nucleation. In view of these conditions, we assume a negligible concentration of nuclei after ingot cool-down and the absence of a time-lag in subsequent nucleation. Consequently, in our model all OPs present after a HT process are nucleated at the beginning of that process. In other publications,^[39–41] the retardation in nucleation is implicitly considered, due to very slow formation of oxygen particles consisting of only several O atoms. Section 5 gives a more detailed discussion of this topic.

The driving force behind oxygen precipitation is an oversaturation with oxygen, which develops during ingot cool-down due to the temperature (and thus time)-dependent solubility limit^[16,22]

$$C_0^*(t) = C_{\text{OI}} e^{-\frac{E_S}{k_B T(t)}} \quad (1)$$

with the constant $C_{\text{OI}} = 9 \times 10^{22} \text{ cm}^{-3}$, the Boltzmann constant k_B, the dissolution enthalpy E_S = 1.52 eV,^[16,42] and the temperature history T(t).

Using Equation (1), the critical radius^[16,22]

$$r_c(t) = \frac{2\sigma}{k_B T(t) \ln \left\{ \frac{C_0}{C_0^*(t)} \right\} C_P} \quad (2)$$

is obtained, describing the time-dependent radius, at which an OP is in equilibrium with its environment. Here, σ and C_P denote the interfacial energy per area and the oxygen density within a precipitate, respectively. Both parameters enter the total free energy at the critical radius,^[16,22]

$$\Delta G(t) = 4\pi\sigma r_c^2(t) - \frac{4}{3}r_c^3(t)\Delta G_v(t) \quad (3)$$

with the volumetric free energy^[16]

$$\Delta G_v(t) = k_B T(t) C_P \ln \left\{ \frac{C_0}{C_0^*(t)} \right\} \quad (4)$$

using which the temperature-dependent density of critical nuclei^[16]

$$N(t) = ce^{-\frac{\Delta G(t)}{k_B T(t)}} \quad (5)$$

during HT processing is obtained. The prefactor c denotes the number of nucleation sites per volume, which equals C_0 under the assumption of a homogenous nucleation mechanism.^[22]

In combination with Equation (2) and (5), the diffusion coefficient of oxygen,^[16,22]

$$D(t) = D_0 e^{-\frac{E_D}{k_B T(t)}} \quad (6)$$

enables the calculation of the process-time-dependent homogeneous nucleation rate^[16,22]

$$J_0(t) = \frac{4\pi C_0 Z}{d} r_c^2(t) D(t) N(t) \quad (7)$$

The parameters entering this result are the oxygen diffusivity $D_0 = 0.13 \text{ cm}^2 \text{ s}^{-1}$, the activation energy for diffusion $E_D = 2.53 \text{ eV}$,^[16,42] the atomic jump distance of oxygen $d = 1.92 \text{ \AA}$,^[17] and the Zeldovich factor Z . The latter is a fitting parameter of our model, describing the ratio of the steady-state density of critical nuclei and their equilibrium density,^[22] where the literature states a value in the range of $0.01^{[16]} \leq Z \leq 0.1^{[22]}$.

In previous research on the nucleation of OPs, σ has been determined to be $38 \times 10^{-6} \text{ J cm}^{-2}$, from the connection between the latent heat of fusion and ΔG_v ,^[22] and $\sigma_1 = 41 \times 10^{-6} \text{ J cm}^{-2}$ from Equation (4) with $C_{P,1} = 2.7 \times 10^{22} \text{ cm}^{-3}$.^[16] However, for large OPs a higher oxygen density of $C_{P,2} = 4.6 \times 10^{22} \text{ cm}^{-3}$ has been used.^[16,17,34] To date, it remains unclear whether C_P stays constant or changes during precipitate growth. A change in atomic density is known from, e.g., the nucleation of water vapor.^[43] In this work, we assume C_P to remain constant during growth and to equal $C_{P,2} = 4.6 \times 10^{22} \text{ cm}^{-3}$, the value known for large OPs. To achieve consistency with literature values, especially in the description of the nucleation, we intend to leave ΔG (Equation (3)) unchanged despite using $C_{P,2}$ instead of $C_{P,1}$. For this purpose, we adapt σ , giving it the values $\sigma_2 = 59.1 \times 10^{-6} \text{ J cm}^{-2}$.

As mentioned, a major influence on the nucleation rate is the time-lag in nucleation, which has been shown for high cooling rates ($> 100 \text{ K h}^{-1}$) following a HT treatment of $> 900^\circ\text{C}$.^[22] However, the lower temperature limit for the appearance of the time-lag is not known to date. In this work, we define the temperature threshold to be 850°C . Consequently, the nucleation rate in our model is taken as $J_0 = 0 \text{ cm}^{-3} \text{ s}^{-1}$ after a HT treatment that fulfills the following two conditions: 1) a peak temperature exceeding 850°C , and 2) a subsequent rapid cooling with a cooling rate higher than 100 K h^{-1} . Note that the present

model disregards cases where the time-lag in nucleation is overcome. This is justified for the purpose of this work, as processes for photovoltaic applications do not resort to extended HT sequences of more than 10 h nor to processes at 450°C of several hours.

As nucleation is the adhesion of an additional oxygen atom, with volume $1/C_P$, to a critical nucleus with radius $r_c^{[22]}$ and as small OPs are approximately spherical,^[16] we define the starting radius of a nucleus right after nucleation as

$$r_c^*(t) = \sqrt[3]{r_c^3(t) + \frac{3}{4\pi C_{P,2}}} \quad (8)$$

Based on Ham's law,^[44] the diffusion-limited surface growth rate of OPs for durations shorter than 50 h is approximated by^[16]

$$\frac{d\{r^2(t)\}}{dt} = 2D(t) \left(\frac{C_0 - C'}{C_P - C'} \right) \quad (9)$$

where C' denotes the temperature-dependent oxygen concentration at the precipitate/silicon interface and is $< 1.6 \times 10^{17} \text{ cm}^{-3}$ for temperatures up to 1050°C .^[16] The materials investigated to evaluate the model of this work exhibit $C_0 \approx 10^{18} \text{ cm}^{-3}$, leading to a maximum influence of C' of 16% in Equation (9). This influence is therefore disregarded, and Equation (9) is simplified to

$$\frac{d\{r^2(t)\}}{dt} = 2D(t) \frac{C_0}{C_P} \quad (10)$$

Diffusion-limited growth can be assumed for precipitate radii $r \gg r_c$. For radii close to the critical radius ($r > r_c$), a retarded growth rate was found.^[45] On the other hand, at $r = r_c$, a precipitate is in equilibrium with its environment, as mentioned, and therefore neither grows nor dissolves. For $r < r_c$, precipitates dissolve until the equilibrium embryo size density distribution is reached, which is described by Equation (5), with r_c replaced by r . The time necessary to transit from a lower temperature distribution to a higher temperature distribution, with correspondingly increasing r_c , is the so-called relaxation or induction time.^[13] The origin of this relaxation time is qualitatively understood, but numerical values were found to differ from experimental observations, which was concluded to result from inadequate assumptions in the corresponding theory.^[22] Therefore, a reliable dissolution rate is also hard to derive. For this reason, in order to account for all growth regimes described above, we introduce the empirical factor $\{1 - (r_c/r)^\gamma\}$ for the diffusion-limited growth (Equation (10)), which leads to a general, size-dependent growth rate of

$$\frac{d\{r^2(t)\}}{dt} = \left\{ 1 - \left(\frac{r_c}{r} \right)^\gamma \right\} 2D(t) \frac{C_0}{C_P} \quad (11)$$

Here, γ is the second fitting parameter of the present model describing the range of nucleus evolutions from dissolution-limited to diffusion-limited growth. Figure 2 shows the empirical factor $\{1 - (r_c/r)^\gamma\}$ plotted versus the normalized precipitate radius, where a normalized growth rate of 1 corresponds to pure diffusion-limited growth (Equation (10)) and negative values correspond to dissolution.

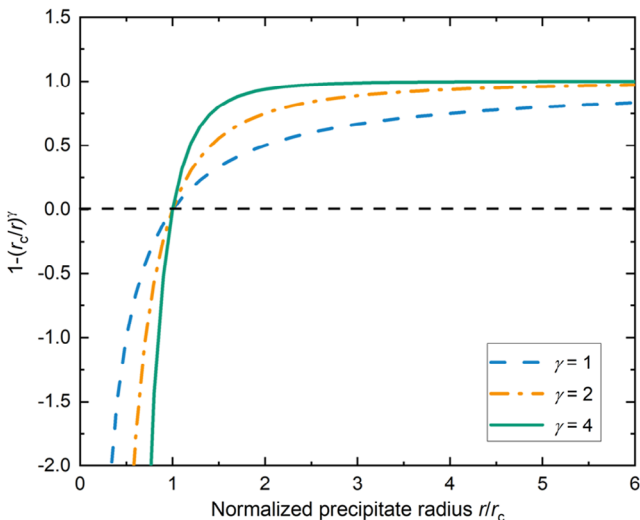


Figure 2. Empirical factor $\{1 - (r_c/r)^\gamma\}$ for the diffusion-limited growth (cf., Equation (11)) plotted versus precipitate radius normalized by the critical radius r_c .

Equation (8) and (11) enable to compute the squared radius of a precipitate at the end of a HT process (t_{end}) which has been nucleated at process time t as

$$r^2(t, t_{\text{end}}) = \max \left\{ 0, r_c^{*2}(t) + \int_t^{t_{\text{end}}} \frac{dr^2(t')}{dt'} dt' \right\} \quad (12)$$

and finally, the total surface area of precipitates per volume using Equation (7) and (12)

$$A_{\text{OP}} = 4\pi \int_{t_0}^{t_{\text{end}}} J_0(t) r^2(t, t_{\text{end}}) dt \quad (13)$$

which is proportional to the recombination activity of OPs. Here, t_0 is the process starting time. Note that the $\max\{\}$ function in Equation (12) is necessary as $dr^2(t)/dt$ can be negative, which can lead to negative values of the integral as well. However, the precipitate shrinking necessarily stops at $r^2 = 0 \text{ cm}^2$.

Using a two-defect SRH model,^[34] the change in bulk recombination rate, due to a HT process j , associated to the growth of OPs

$$\Delta R_{\text{B,SRH},j} = \tau_{\text{SRH}}^{-1} = \tau_{\text{SRH},1}^{-1} + \tau_{\text{SRH},2}^{-1} \quad (14)$$

is calculated, where the SRH lifetime (for p- and n-type silicon) is^[46]

Table 1. SRH parameters for calculating the lifetime limit due to oxygen precipitation according to the two-defect model of Murphy et al.^[34] The adapted energy level for OP defect 2 is taken from ref. [41].

Recombination center	Energy level E_T [eV]	Electron recombination velocity S_n [cm s ⁻¹]	Hole recombination velocity S_p [cm s ⁻¹]	S_n/S_p
OP Defect 1	$E_V + 0.22$	1.3×10^6	8.0×10^3	1.57×10^2
OP Defect 2	$E_C - 0.14$	6.7×10^3	8.0×10^6	8.33×10^{-4}

$$\tau_{\text{SRH},i} = \frac{\tau_{p0,i}(n_0 + n_{1,i} + \Delta n) + \tau_{n0,i}(p_0 + p_{1,i} + \Delta n)}{n_0 + p_0 + \Delta n} \quad (15)$$

and $i = 1, 2$ denotes the two relevant defects. Equation (15) is valid under the assumption of negligible trapping and, hence, identical excess electron and hole concentrations ($\Delta n = \Delta p$). Here, p_0 and n_0 denote the equilibrium hole and electron densities, while the densities $p_{1,i}$ and $n_{1,i}$ are the equilibrium densities when the defect energy level $E_{T,i}$ coincides with the Fermi level^[47]

$$p_{1,i} = N_V e^{\left(-\frac{E_{T,i} - E_V}{k_B T} \right)}; n_{1,i} = N_C e^{\left(-\frac{E_C - E_{T,i}}{k_B T} \right)} \quad (16)$$

Values for the effective densities of states in the conduction and valence band at 300 K are $N_C = 2.86 \times 10^{19} \text{ cm}^{-3}$ and $N_V = 3.10 \times 10^{19} \text{ cm}^{-3}$.^[47,48]

Finally, parameters $\tau_{p0,i}$ and $\tau_{n0,i}$ link the calculated A_{OP} (see Equation (13)) with the recombination velocities at the precipitate–silicon interface $S_{p,i}$ and $S_{n,i}$.^[34] respectively

$$\tau_{p0,i} = (S_{p,i} A_{\text{OP}})^{-1}; \tau_{n0,i} = (S_{n,i} A_{\text{OP}})^{-1} \quad (17)$$

Table 1 lists the used SRH parameters. All parameters are taken from Murphy et al.,^[34] except the energy level of OP defect 1 which we found to match better for the description of recombination in our samples.^[41]

In order to calibrate the present model in this section, the two free parameters Z and γ need to be found. This is the aim of the experiments described in the next section.

3. Experimental Section

This section presents three experiments in which the nucleation, growth, and dissolution of OPs are analyzed separately on the level of symmetrical carrier lifetime samples. Some of this data is used to calibrate the model (Section 3.1–3.3). In a fourth experiment, the model is validated using PERCs (Section 3.4).

Overall, pseudo-square-shaped large-area wafers from nine different Cz-Si materials, delivered by five providers, are investigated. **Table 2** gives an overview of the materials and relates them to the performed experiments. For the symmetrical carrier lifetime samples (Section 3.1–3.3), at least four materials are considered in each experiment. They are taken from two boron-doped p-type Cz-Si materials and two phosphorus-doped n-type Cz-Si materials, containing either high or low concentrations of TDs (pCz-high[TD]; pCz-low[TD]; nCz-high[TD], and nCz-low[TD]). The PERCs (Section 3.4) are based on gallium-doped p-type Cz-Si material, which has become the new standard in p-type solar cell manufacturing.^[6]

Table 2. Overview of the 156 mm-edge-length wafers used in the four experiments focusing on nucleation (Nuc.), growth (Growth), and dissolution (Diss.) of OPs as well as on PERC manufacturing. Besides a relation of the materials to each experiment, the resistivities $\rho_{B,1}$ and $\rho_{B,2}$ before and after HT treatment (i.e., TD annihilation), respectively, are listed. The indicated concentrations C_{TD} of TDs are derived from these resistivities according to ref. [26]. Also, the measured oxygen concentrations C_0 are given. For materials without existing measurement, C_0 values are obtained by a fit of measured C_0 from the other materials versus C_{TD} values (marked with “Fit”). Both “pCz-low[TD]” materials are produced by the magnetic Czochralski (mCz) technology.^[61]

Material	Provider	Type	Dopant	$\rho_{B,1}$ [$\Omega \text{ cm}$]	$\rho_{B,2}$ [$\Omega \text{ cm}$]	C_{TD} [10^{14} cm^{-3}]	C_0 [10^{17} cm^{-3}]	Investigated in experiment			
								Nuc.	Growth	Diss.	PERC
pCz-PERC	A	p-type Cz-Si	Ga	5.2	2.3	15.7	11.0 ± 2.7 (Fit)	–	–	–	X
pCz-high[TD]-1	A	p-type Cz-Si	B	3.2	2.0	11.2	9.5 ± 0.4	X	X	X	–
pCz-low[TD]-1	B	p-type mCz-Si	B	0.6	0.6	0.1	2.5 ± 0.4	X	X	–	–
pCz-low[TD]-2	B	p-type mCz-Si	B	1.3	1.2	0.3	3.7 ± 0.9 (Fit)	–	–	X	–
nCz-high[TD]-1	C	n-type Cz-Si	P	1.2	3.0	13.5	10.6 ± 2.6 (Fit)	X	–	X	–
nCz-high[TD]-2	D	n-type Cz-Si	P	2.0	10.5	10.1	11.2 ± 0.6	–	X	–	–
nCz-low[TD]-1	E	n-type Cz-Si	P	5.5	6.1	0.4	4.0 ± 1.0 (Fit)	X	–	–	–
nCz-low[TD]-2	E	n-type Cz-Si	P	5.4	5.9	0.4	4.2 ± 0.3	–	X	–	–
nCz-low[TD]-3	E	n-type Cz-Si	P	4.7	6.0	1.1	5.3 ± 1.3 (Fit)	–	–	X	–

3.1. Nucleation of Oxygen Precipitates

The manufacturing process flow for the symmetrical carrier lifetime samples to investigate the influence of HT process parameters on the nucleation of OPs is shown in Figure 3 (left). After a saw damage etch and a wet chemical cleaning treatment in hydrogen chloride (HCl) as the first of two cleaning steps, a sheet resistance (R_{sh}) measurement by the eddy-current technique and a capacitive wafer thickness measurement are carried out on all wafers. The data allow to obtain the as-grown resistivities $\rho_{B,1}$, which could be affected by the presence of TDs. After the second cleaning step in hydrofluoric acid (HF), variations of the POCl_3 diffusion process parameters are performed with a group size of three wafers of each material as described below. All wafers then undergo phosphor silicate glass (PSG) etching and an alkaline wet chemical etch to remove the diffused region. Thereafter, a second round of R_{sh} and capacitive wafer thickness measurements allows to calculate $\rho_{B,2}$ after TD annihilation during the

diffusion process. The two measurements $\rho_{B,1}$ and $\rho_{B,2}$ yield the TD concentration C_{TD} according to ref. [27]. This method takes the influence of the stronger carrier scattering by TDs and of reduced charge mobility due to potential charge carrier compensation into account.^[26] Next, the wafers are passivated with a both-sided deposition of a 20 nm-thick Al_2O_3 layer by atomic layer deposition (ALD), in view of subsequent carrier lifetime and PL measurements. A 10 min-long forming gas anneal (FGA) at 400 °C in a tube furnace activates the surface passivation. Due to the short duration of the FGA, we do not expect the time-lag in nucleation to be overcome as a consequence of TD formation, where the literature states a necessary duration of several hours.^[22] To keep the illumination-sensitive boron-oxygen defects in the deactivated state,^[49] and hence to avoid their detrimental impact on bulk lifetime, all carrier lifetime samples are stored in the dark after passivation until the subsequent measurements. All carrier lifetime samples manufactured in this work underwent the same procedure. PL imaging is

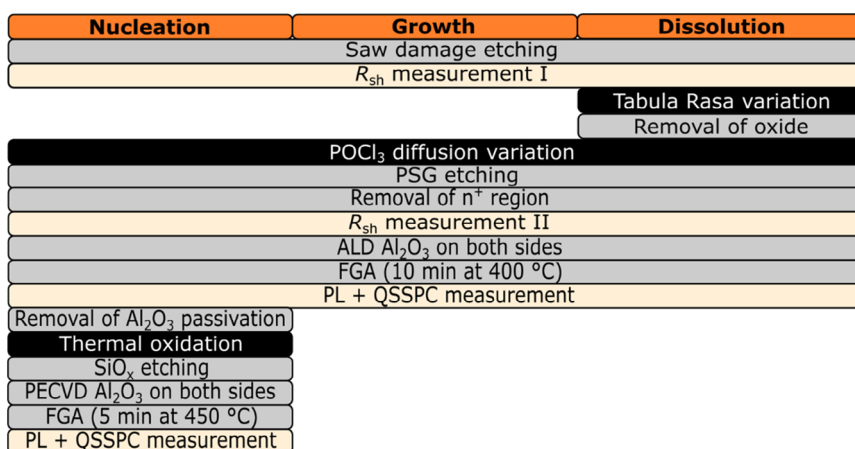


Figure 3. Process flow for manufacturing symmetric carrier lifetime samples fabricated in nucleation (left, this section), growth (middle, Section 3.2), and dissolution experiment (right, Section 3.3). The HT processes, influencing OP formation, as well as the performed measurements are highlighted in black and yellow, respectively.

applied to determine the qualitative lifetime distribution and quasi-steady-state photoconductance decay (QSSPC) lifetime measurements performed at five positions per wafer serve to determine the average effective carrier lifetime τ_{eff} . Note that τ_{eff} is a measured value, while τ_{SRH} denotes the modeled bulk lifetime limitation due to oxygen precipitation, which is calculated according to Equation (15). The effective lifetimes are evaluated at a fixed excess carrier concentration of 10^{15} cm^{-3} . As no circular defect pattern in PL nor significant differences in τ_{eff} were found for any sample of this experiment (not shown in this work), the Al_2O_3 passivation layer is removed in HF and after a wet chemical cleaning a 40 min-long thermal oxidation process at 850°C (Ox1, see **Table 3**) is performed as a second HT process. This process is conducted for further growth of the OPs already

present in the samples. We expect the OP density after the first HT process to remain unaffected by this process, due, on the one hand, to the time-lag in nucleation and, on the other hand, to the lower peak temperature of the oxidation process compared to the POCl_3 diffusion variations, which prevents OPs from dissolving. All wafers then undergo an HF etch to remove the thermal oxide and are again passivated by a both-sided deposition of a 40 nm-thick Al_2O_3 layer by plasma-enhanced chemical vapor deposition (PECVD). After a 5 min-long FGA at 450°C in a tube furnace to activate the passivation, PL imaging and QSSPC measurements are again performed. Note that both, Al_2O_3 deposition method and FGA process recipe differ from the passivation procedure performed previously (cf., Figure 3) for reason of ALD process unavailability. Therefore, a potential difference in bulk

Table 3. Overview of the process parameters of the investigated POCl_3 diffusion, thermal oxidation, and Tabula Rasa processes of all four experiments performed in this work: temperature at process start T_{start} ; durations t_{dep} and t_{drive} as well as temperatures T_{dep} and T_{drive} of the deposition and drive-in (respectively oxidation) sequence, respectively; slopes of the temperature ramps, a_{dep} and a_{drive} , toward the deposition and drive-in plateaus, respectively; gas atmosphere. Nuc., nucleation experiment; Growth, growth experiment; Diss., dissolution experiment; PERC, PERC manufacturing.

Process	Experiment	Deposition				Drive-in resp. oxidation			
		T_{start} [°C]	a_{dep} [K min^{-1}]	T_{dep} [°C]	t_{dep} [min]	a_{drive} [K min^{-1}]	T_{drive} [°C]	t_{drive} [min]	Gas
P0	Nuc.; Growth	≈650	≥ 10	794	28	—	—	—	—
P1	Nuc.	≈650	≥ 10	794	28	≈5	860	35	O_2
P2	Nuc.	≈750	≥ 10	794	28	≈5	860	35	O_2
P3	Nuc.	≈650	≥ 10	794	28	≈10	860	37	O_2
P4	Nuc.	≈650	≥ 10	794	18	≈5	860	37	O_2
P5	Nuc.	≈650	≥ 10	794	63	≈5	860	28	O_2
P6	Nuc.	≈650	≥ 10	760	28	≈5	860	37	O_2
P7	Nuc.	≈650	≥ 10	794	18	≈10	860	40	O_2
P8	Nuc.	≈650	≥ 10	860	43	—	—	—	O_2
P9	Nuc.	≈650	≥ 10	860	18	≈-3	830	51	O_2
P10	Nuc.	≈650	≈5	860	40	—	—	—	O_2
P11	Nuc.	≈650	≥ 10	794	28	≈10	900	5	O_2
P12	Growth; PERC	≈650	≥ 10	794	28	≈5	860	17	O_2
P13	Growth; Diss	≈650	≥ 10	794	28	≈5	860	125	O_2
P14	Growth	≈650	≥ 10	794	28	≈5	1050	17	O_2
P15	Growth	≈650	≥ 10	794	28	≈5	1050	125	O_2
P16	Growth	≈650	≥ 10	794	28	≈5	860	17	N_2
P17	Growth	≈650	≥ 10	794	28	≈5	860	125	N_2
P18	Growth	≈650	≥ 10	794	28	≈5	1050	17	N_2
P19	Growth	≈650	≥ 10	794	28	≈5	1050	125	N_2
P20	Diss.	≈650	≥ 10	770	30	≈10	950	35	N_2
P21	PERC	≈650	≥ 10	794	28	≈5	860	11	O_2
P22	PERC	≈650	≥ 10	794	28	≈5	860	23	O_2
P23	PERC	≈650	≥ 10	798	28	≈5	860	17	O_2
Ox1	Nuc.	≈700	—	—	—	≈10	850	40	O_2
Ox2	PERC	≈700	—	—	—	≈10	800	36	O_2
Ox3	PERC	≈700	—	—	—	≈10	850	20	O_2
Ox4	PERC	≈700	—	—	—	≈10	900	15	O_2
TR1000	Diss.	≈745	—	—	—	≈10	1000	20	O_2/DCE
TR1050	Diss.	≈745	—	—	—	≈10	1050	20	O_2/DCE

hydrogenation, and as a consequence in the degree of OP passivation, based on the usage of a PECVD instead of an ALD tool as hypothesized in ref. [50] cannot be ruled out.

Next, the POCl_3 diffusion processes performed in the nucleation experiment are described. Hereby, a variation of 11 POCl_3 diffusion processes (P1–P11) and a reference process (P0) are performed in an industrial tube furnace. Figure 4 schematically shows the thermal history of these 12 processes. The first temperature plateau represents the deposition and growth sequence of the PSG layer, in the following denoted as deposition sequence, while the second plateau represents the so-called drive-in sequence, in which the main phosphorus diffusion from the PSG layer into the silicon bulk takes place. The reference process P0 consists of a 28 min-long deposition at 794°C only, based on the deposition sequence of an industrially relevant PERC manufacturing process.^[51] P0 is intended to lead to a first phosphorus diffusion gettering (PDG),^[52–55] reducing possible differences in concentration of metallic impurities between P0 and the POCl_3 diffusion processes $j = \{\text{P1}, \text{P2}, \dots\}$, while negligible growth of OPs is expected for P0. This reference process P0 enables to determine the change in bulk recombination rate that we define as

$$\Delta R_{B,j} = \frac{1}{\tau_{\text{eff},j}} - \frac{1}{\tau_{\text{eff},\text{P0}}} \quad (18)$$

Thereby, further influences are mathematically eliminated. Such influences include Auger recombination as well as surface recombination, when the same surface passivation is used for samples processed using P0 and POCl_3 diffusion process j . Here, $\tau_{\text{eff},j}$ and $\tau_{\text{eff},\text{P0}}$ denote the average effective lifetime of each variation j and of the reference process P0, respectively. $\Delta R_{B,j}$ values are obtained by averaging over three samples per group with five measurements per sample. Note that it is also possible for $\Delta R_{B,j}$ to take negative values, e.g., when POCl_3 diffusion process j leads to a more effective PDG than reference process P0. It is noteworthy that reference samples subjected to P0 are not

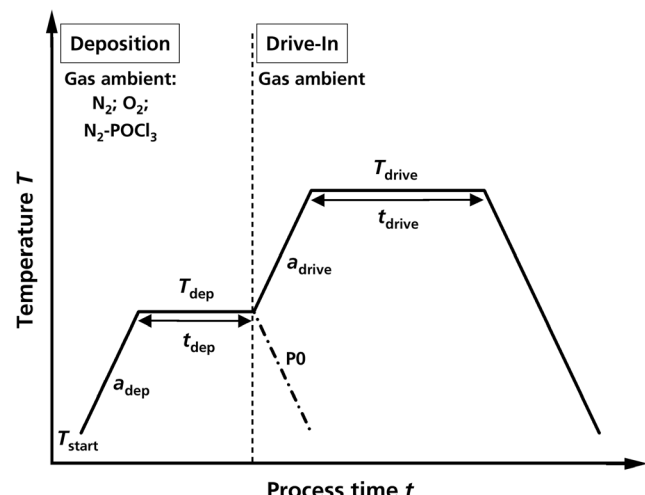


Figure 4. Schematic temperature–time profile of a two-temperature-plateau POCl_3 diffusion process as well as reference process P0. Depicted process parameters are defined for each diffusion process in Table 3.

subjected to the thermal oxidation process, while being processed identically to the POCl_3 diffusion variation samples regarding all other process steps reported in Figure 3, especially regarding surface passivation.

The 11 POCl_3 diffusion process variations are designed to analyze the impact of the 1) temperature T_{start} at the process start (the moment when tube door is closed), 2) duration t_{dep} and temperature T_{dep} of the deposition plateau, 3) duration t_{drive} and temperature T_{drive} of the drive-in plateau, 4) slopes of the temperature ramps, a_{dep} and a_{drive} , toward the deposition and drive-in plateaus, respectively, on oxygen precipitation (for details, see Table 3 and Figure 4). The duration t_{drive} is adapted so that the interstitial oxygen diffusion length $L_{\text{O}_{\text{i}},j}$ is similar for all investigated processes $j = \{\text{P1}, \text{P2}, \dots\}$. $L_{\text{O}_{\text{i}},j}$ is derived from Equation (10) as follows

$$r_j^2(t_0, t_{\text{end}}) \approx 2 \frac{C_0}{C_p} \int_{t_0}^{t_{\text{end}}} D_j(t') dt' = 2 \frac{C_0}{C_p} L_{\text{O}_{\text{i}},j}^2 \quad (19)$$

where t_0 and t_{end} denote the process starting and ending times and $D_j(t)$ represents the thermal history of the sample via the time dependent oxygen diffusion coefficient of process j . Equation (19) leads to

$$L_{\text{O}_{\text{i}},j} = \sqrt{\int_{t_0}^{t_{\text{end}}} D_j(t') dt'} \quad (20)$$

Hence, $L_{\text{O}_{\text{i}},j}$ is proportional to the diffusion-limited growth of OPs during HT process j . Note that we corrected the calculation of $L_{\text{O}_{\text{i}}}$ presented in our previous work.^[56] Due to an identical $L_{\text{O}_{\text{i}}}$ of different processes, the size of a precipitate, nucleated in the beginning of each process, is equal when the processes are completed (neglecting possible differences due to the retarded growth of small OPs). Hence, the performed adaption of t_{drive} for each process equalizes the growth during the different processes. Due to this procedure, differences in ΔR_B predominantly originate from a different OP density and therefore a different nucleation during the processes. After the POCl_3 diffusion process variations, we calculate $L_{\text{O}_{\text{i}},j} = 0.41 \pm 0.01 \mu\text{m}$ from Equation (20). After thermal oxidation, $L_{\text{O}_{\text{i}},j} = 0.66 \pm 0.01 \mu\text{m}$ is obtained. Section 4.2 considers the correlation between $L_{\text{O}_{\text{i}}}$ and the growth of OPs in more detail.

Table 3 shows an overview of the process parameters of the investigated POCl_3 diffusion processes P1–P11. In all cases, the temperature ramps up to the deposition plateau are performed in pure nitrogen. Then a POCl_3 -rich N_2/O_2 gas composition is introduced for 15 min to grow the PSG layer, before the furnace is flushed for 3 min with pure nitrogen. Then a gas ambient consisting of 100% O_2 is introduced, which is maintained until the end of the deposition sequence and further until the unloading temperature is reached. The only exception is process P5, which comprises a long deposition sequence of $t_{\text{dep}} = 63$ min. Hereby, the 15 min-long phase with the POCl_3 -rich gas, followed by the 3 min-long flush with pure nitrogen, starts only after the deposition temperature was already kept constant for 45 min in pure nitrogen. For all processes, the slopes of the final cool-down ramps are $\geq 180 \text{ K h}^{-1}$.

3.2. Growth of Oxygen Precipitates

Results of this experiment have already been presented in refs. [41,57]. These results are briefly summarized here because they serve to calibrate the model.

Symmetrical carrier lifetime samples for investigating the growth of OPs separately from nucleation are manufactured according to the process flow depicted in Figure 3 (middle). In contrast to the nucleation experiment of Section 3.1, a variation of POCl_3 diffusion processes is performed without using subsequent thermal oxidation. Therefore, wafers from four different materials (cf., Table 2) are processed until after the first PL and QSSPC measurements. In addition, selected samples are analyzed using Fourier-transform infrared (FTIR) spectroscopy to determine the interstitial oxygen concentration C_0 as well as the loss ΔC_0 due to HT processing. Furthermore, optical microscopy serves to determine the density of etch pits formed using a Secco etch.

The performed POCl_3 diffusion processes (P12–P19) in this batch consist of eight variations of the process outlined in Figure 4 and the additional reference process P0, for calculating ΔR_B using Equation (18). Here, three wafers per material and process are investigated. Table 3 gives an overview of the process parameters of processes P12–P19. All variations include the same deposition sequence as the reference process P0. After deposition, the temperature is ramped up to the drive-in temperature plateau. Variations concern T_{drive} (860 or 1050 °C) and t_{drive} (17 and 125 min), which results in four combinations. The variations are performed in oxidizing (P12–P15) or inert (P16–P19) atmospheres, which are kept constant from tube flushing after deposition until the unloading temperature is reached. Note that P12 is relevant for industrial PERC manufacturing.^[51] The reason for the variation of the drive-in atmosphere was to investigate its influence on the growth of OPs during POCl_3 diffusion. The variation of T_{drive} and t_{drive} leads to a wide spectrum in oxygen diffusion length of $0.4 \mu\text{m} \leq L_{\text{O}_{i,j}} \leq 5.2 \mu\text{m}$, which should cover a wide range of HT processes relevant for photovoltaic applications. As the deposition sequence and a_{drive} are identical for all variations, the density of OPs is expected to be similar. Therefore, changes in ΔR_B can be attributed to a difference in OP size.

3.3. Dissolution of Oxygen Precipitates

To investigate the dissolution behavior of nuclei and small OPs, TR treatments are performed using wafers from four materials (cf., Table 2). The process flow for manufacturing symmetrical carrier lifetime samples is depicted in Figure 3 (right) and includes all process steps described in Section 3.2. In addition, a variation of TR preconditioning processes is performed before the POCl_3 diffusion variation. After the saw damage etch and the first R_{sh} measurement, all wafers are wet chemically cleaned and the TR variation is performed in an industrial tube furnace. The thermal oxide, formed during the TR processes, is then removed in HF followed by the POCl_3 diffusion variation and the remaining process steps.

Two TR processes are performed, consisting of a single-temperature-plateau process with a temperature plateau at either

1000 °C (TR1000) or 1050 °C (TR1050), where 1050 °C is the temperature limit of the used tube furnace. Table 3 gives an overview of the process parameters. Except for the temperature, both processes are identical in terms of gas atmosphere and slopes of the positive and negative temperature ramps. The temperature is ramped up to the plateau value at about 10 K min^{-1} , which is then kept for 20 min. From the start of the process until the end of the temperature plateau, an oxidizing gas atmosphere is applied, consisting of O_2 with a minor percentage of dichloroethylene (DCE) to capture metallic impurities. During the temperature ramp-down (at $\approx 300 \text{ K h}^{-1}$), the gas atmosphere consists of pure nitrogen. In addition, a reference group is considered, which does not undergo a TR process (noTR).

The POCl_3 diffusion variation includes the POCl_3 diffusion processes P13 and P20 (cf., Table 3) as well as the absence of POCl_3 diffusion (noDiff). The three groups of the TR variation (TR1000, TR1050, and noTR) as well as the three groups of the POCl_3 diffusion process variation (P13, P20, and noDiff) are conducted in a full factorial design of experiment, leading to nine combinations. One of these includes no HT process at all, which represents a reference group in this experiment. Again, three wafers per material and process variation are investigated. In contrast with Section 3.1 and 3.2, the reference process P0 is not performed. To allow the comparison of the different experiments and, hence, to calculate ΔR_B by Equation (18) for materials pCz-high[TD]-1 and nCz-high[TD]-1, the QSSPC measurements after process P0 (passivated using ALD Al_2O_3) from Section 3.1 are used. This seems a viable approach, as the same materials (cf., Table 2) as well as the same passivation sequence are used in both experiments, although the samples were not processed in the same batch.

3.4. Manufacturing of PERCs

To investigate the impact of OPs on cell efficiency, we manufactured PERCs using wafers of material pCz-PERC (see Table 2). The process flow for PERC manufacturing is based on the Fraunhofer ISE PVTEC baseline^[57] with slight modifications regarding rear surface passivation, where a PECVD silicon oxide (SiO_x) layer is used instead of aluminum oxide (AlO_x). Figure 5 shows the used process flow for the individual groups of this experiment. After alkaline texturing, a variation of POCl_3 diffusion processes is performed. Subsequently, an inline wet

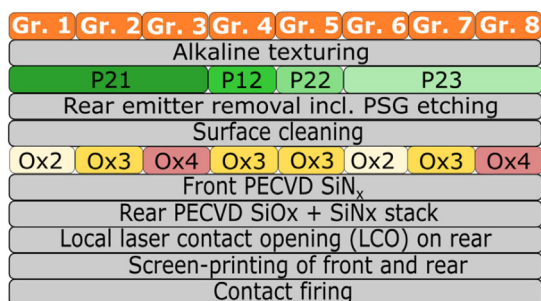


Figure 5. Process flow for the manufacturing of PERCs. The HT processes, influencing OP formation, are highlighted and the process parameters are listed in Table 3.

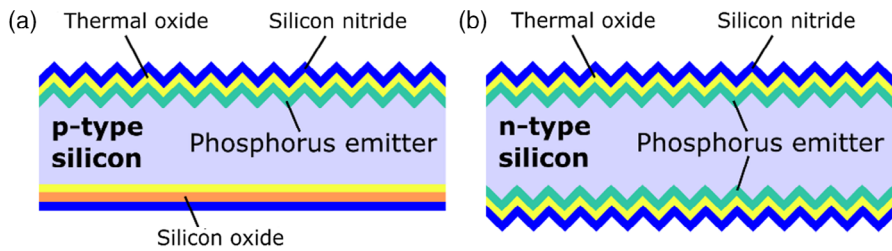


Figure 6. Schematic cross section of a) a nonmetallized cell test structure before back etching and b) a symmetrical sample to determine the dark saturation current density j_{oe} .

chemical etching process removes the rear emitter and the front PSG layer. Wet chemical cleaning is then followed by a variation of thermal oxidation processes. To complete surface passivation, a 65 nm-thick silicon nitride layer (SiN_x) is deposited on the front side and a stack consisting of a 150 nm-thick PECVD SiO_x layer capped by a 150 nm-thick PECVD SiN_x layer is deposited on the rear. After a local contact opening (LCO) of the rear passivation via laser ablation, a full aluminum metallization (without silver pads) is screen-printed. For the front side metallization, a zero-busbar screen layout is used. Finally, contact firing is performed in a conveyor belt furnace and the cells are measured using an in-house current–voltage (I – V) tester.

In addition to the PERCs, nonmetallized cell test structures are prepared as well. These cell test structures are manufactured analogously to the PERCs. However, the LCO and metallization processes are skipped. **Figure 6a** shows a schematic cross section of this sample structure at the end of the fabrication process after firing. In the next step, these samples are etched in HF and KOH to remove the passivation layers and the diffused emitter, respectively. Then, the samples are cleaned and repassivated using a both-sided 40 nm-thick PECVD Al_2O_3 layer, where the passivation is activated due to a subsequent 5 min-long FGA at 450 °C. The resulting symmetrical carrier lifetime samples enable to investigate a potential impact of the HT process sequence on the bulk carrier lifetime more clearly. A PL imaging is performed to investigate the lifetime distribution of these samples. Furthermore, QSSPC measurements yield the effective lifetime τ_{eff} , which approximates the bulk carrier lifetime due to negligible surface recombination. The QSSPC measurements on these symmetrical carrier lifetime samples also yield the implied open-circuit voltage limit $iV_{OC,bulk}$ due to bulk recombination. As the used material is gallium-doped, boron–oxygen defects cannot be formed due to illumination. Nevertheless, these samples are stored in the dark until the measurements, like the samples of Section 3.1–3.3.

Furthermore, symmetrical samples to determine the emitter dark saturation current density j_{oe} are manufactured using wafers of material nCz-low[TD]-2 (see Table 2). These samples are processed as depicted in Figure 5 up to and including thermal oxidation. However, the wet chemical etching process to remove the rear emitter is left out and only the PSG is removed on both sides. After thermal oxidation, the PECVD SiN_x layer serving for the front side passivation of the PERCs is deposited on both sides. **Figure 6b** shows a schematic cross section. Finally, the samples are fired and characterized using QSSPC. Based on

these measurements, j_{oe} is evaluated using the method of Kane and Swanson^[58] refined by Kimmerle et al.^[59]

Using all three types of samples (PERCs; nonmetallized cell test structures; j_{oe} samples), eight different combinations of POCl_3 diffusion and thermal oxidization processes are investigated (cf., Figure 5). Based on process P12 (see Table 3), a variation of the duration of the drive-in plateau (P21–P22) as well as of the deposition plateau temperature (P23) is performed while keeping all other process parameters unchanged. After processes P12 and P22, a thermal oxidation Ox3 is carried out at 850 °C for 20 min. In addition, two more oxidation processes, at 800 °C for 36 min (Ox2) as well as at 900 °C for 15 min (Ox4), are applied for sample groups processed using P21 and P23. An overview of the process parameters for these thermal oxidation processes is given in Table 3. The duration of the temperature plateaus is adapted to ensure thermal oxides of similar thickness. Besides the duration and temperature of the plateau, all other process parameters of these three processes, such as gas atmosphere and slopes of temperature ramps, are identical.

4. Results

To calibrate the model, the results of material pCz-high[TD]-1 of the nucleation, growth, and dissolution experiments (Section 4.1–4.3) are used. This material is used for calibration as it was processed in all experiments and a measurement of its C_0 is available (cf., Table 2). However, the results of the nucleation experiment achieved without a subsequent thermal oxidation process are excluded from calibration as no defect patterns have been found, as explained above. Furthermore, as a low PL signal in the wafer corners of unknown origin is found after TR treatments (cf., Section 4.3), the TR processes are also excluded from calibration. For calculation of ΔR_B for processes P13 and P20 of the dissolution experiment, we used reference process P0 of the nucleation experiment, as described in Section 3.3. The results of processes P13 and P17 of the growth experiment were not used for calibration because a strong influence due to metallic contamination is surmised for the corresponding samples (cf., Section 4.2). This is also stated in ref. [41]. The selective exclusions still leave samples exposed to 19 different process histories for calibrating the model.

For calibration of the model, a logarithmic fit of the two free parameters Z and γ is performed to maximize the coefficient of determination R^2 according to

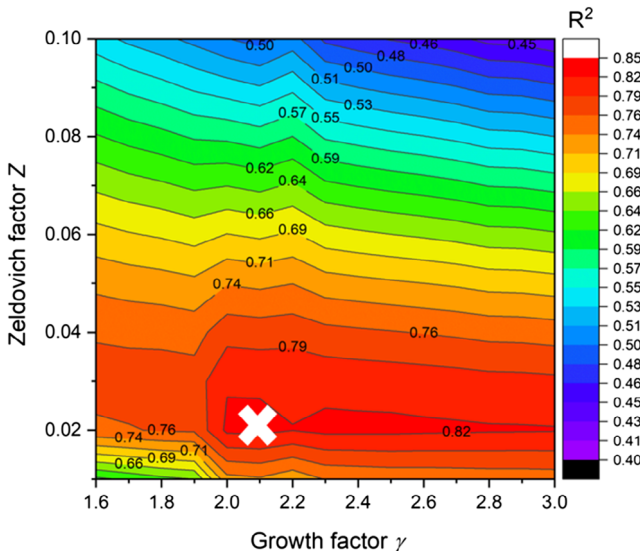


Figure 7. Coefficient of determination R^2 (see Equation (21)) as a function of the free parameters, i.e., the Zeldovich factor Z and growth factor γ . The position of the maximum $R^2 = 0.83$ is indicated by a white cross.

$$R^2 = 1 - \frac{\sum_j \{ \log(\Delta R_{B,j}) - \log(\Delta R_{B,SRH,j}) \}^2}{\sum_j \{ \log(\Delta R_{B,j}) - \overline{\log(\Delta R_B)} \}^2} \quad (21)$$

with the experimental data $\Delta R_{B,j}$ from Equation (18) and the predicted data from the model $\Delta R_{B,SRH,j}$ from Equation (15) in units of μs^{-1} . In Figure 7, the results for R^2 for the varied free parameters are shown. The highest agreement with $R^2 = 0.83$ was found for $Z = 0.02$ and $\gamma = 2.1$.

Calculations performed in this work are executed with a discretization of the HT process time in steps of $\Delta t = 1$ min. The question of convergence of the computation with Δt deserved special attention. To examine the influence of Δt , we computed selected processes using $\Delta t = 2$ min as well as $\Delta t = 4$ min and indeed found an impact of Δt . This impact is dominated by the exponential dependence of the oxygen diffusion coefficient of oxygen D (see Equation (6)), which is of central importance for the calculation of the OP growth rate (see Equation (11)). At the temperature ramps up and down, the exponential behavior of $D(t)$ leads to an underestimation of the OP growth rate due to the discretization. Consequently, a larger Δt results in a stronger underestimation of the OP size and hence of the total OP surface area A_{OP} (see Equation (13)). For the calculation using $\Delta t = 4$ min, the underestimate amounts to about 25% in comparison to $\Delta t = 1$ min. For $\Delta t = 2$ min, the underestimate is about 5%. Therefore, we expect the further convergence at Δt tending to 0 to be small. In the interest of computational efficiency, all numerical integration were thus carried out with $\Delta t = 1$ min.

4.1. Nucleation of Oxygen Precipitates

In Table 2, the measured resistivities before ($\rho_{B,1}$) and after ($\rho_{B,2}$) HT treatment, the calculated C_{TD} values as well as C_0 are listed for all investigated materials. For materials pCz-high[TD]-1 and

pCz-low[TD]-1, C_0 is measured on neighboring wafers in the growth experiment. The value of C_0 of materials nCz-high[TD]-1 as well as nCz-low[TD]-1 is estimated using a fit function of the measured C_0 of the other investigated materials (see Table 2) over C_{TD} because no FTIR measurement is available for these materials. This fit is feasible under the assumption of identical ingot cool-down and hence identical duration in the TD formation temperature regime. The larger errors stated in Table 2 represent the higher uncertainty of this estimation procedure compared to the C_0 values extracted from FTIR measurements.

After the POCl_3 diffusion variation as a first HT treatment, no circular defect pattern was found in the PL images taken after passivation in any investigated materials processed as described in Section 3.1. After increasing L_{O_i} (and therefore OP growth) due to the oxidation process Ox1 as a second HT treatment, defect patterns are visible on both “high[TD]” materials but differ between the varied POCl_3 diffusion processes. On neither of the two “low[TD]” materials is any defect pattern visible even after

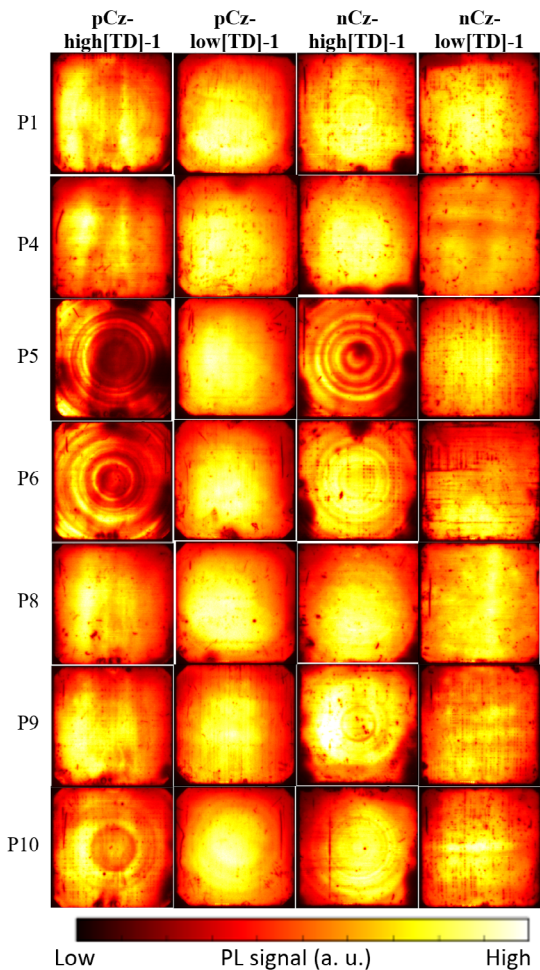


Figure 8. Individually scaled PL measurements of one representative symmetrical carrier lifetime sample for each of the four investigated materials in the nucleation experiment, processed using selected POCl_3 diffusion process variations followed by thermal oxidation Ox1 (see Table 3).

the second HT treatment, which confirms the correlation between C_{TD} and the susceptibility of a material to form OPs.

In Figure 8, PL results of samples from selected processes are shown for all investigated materials. Note that all measurements are scaled individually to see the contours of the circular defect pattern of each sample more clearly. For both “high[TD]” materials, circular defect patterns show most strongly for processes P5 ($T_{dep} = 794^\circ\text{C}$; $t_{dep} = 63\text{ min}$) and P6 ($T_{dep} = 760^\circ\text{C}$; $t_{dep} = 28\text{ min}$). The comparison of these processes with P1 ($T_{dep} = 794^\circ\text{C}$; $t_{dep} = 28\text{ min}$) and P4 ($T_{dep} = 794^\circ\text{C}$; $t_{dep} = 18\text{ min}$) is of major interest because all process parameters except T_{dep} , t_{dep} , and t_{drive} are kept constant. As explained in Section 3.1, t_{drive} was adapted with the sole purpose of yielding similar precipitate growth. This comparison leads to the conclusion that the temperature and duration of the deposition sequence are highly relevant to influence the strength of the defect pattern in this experiment. This strength increases with increasing duration t_{dep} and decreasing temperature T_{dep} . This inverse correlation with T_{dep} is also confirmed by the absence of defect pattern after single plateau process P8 ($T_{dep} = 860^\circ\text{C}$; $t_{dep} = 43\text{ min}$). Assuming equivalent OP growth, the correlations with t_{dep} and T_{dep} are explained by the change in OP density and therefore in a different nucleation intensity of the applied processes. The nucleation rate increases when T_{dep} approximates the peak nucleation temperature at about 750°C .^[13,16,17] The number of formed nuclei increases with duration within the nucleation temperature range and hence with increasing t_{dep} . Note that for process P5, with a 45 min-long period in N_2 ambient before starting the growth of the PSG layer as mentioned in Section 3.1, an N_2 -induced enhanced nucleation rate cannot be excluded.

The results of process P10 (cf., Figure 8) support the finding of an enhanced nucleation due to a longer duration in the nucleation temperature range, where a decreased temperature ramp of $a_{dep} \approx 5\text{ K min}^{-1}$ in comparison with $a_{dep} \geq 10\text{ K min}^{-1}$ of process P8 leads to a formation of weak defect patterns for both “high[TD]” materials.

Another important observation is that the two-temperature-plateau process P9 ($T_{dep} = 860^\circ\text{C}$; $T_{drive} = 830^\circ\text{C}$) does not show any circular defect pattern in pCz-high[TD]-1 material, while a weak pattern is visible for nCz-high[TD]-1. Neither material shows this pattern after a single temperature plateau at 860°C (process P8) although L_{O_i} and thus OP growth is similar. We therefore see no reason to assume the development of a time-lag in nucleation due to the 30 K decrease from deposition to drive-in plateau of process P9.

Finally, none of the processes P2, P3, P7, and P11 (not shown in Figure 8) shows circular defect pattern in any investigated material. Therefore, no conclusion can be drawn at this point regarding the impact of a steeper a_{drive} (comparison between P3 and P1 as well as between P7 and P4), starting temperature T_{start} (comparison between P2 and P1), as well as higher dissolution due to a higher T_{drive} (comparison between P11 and P3). If L_{O_i} and thus OP growth are further increased, differences between these processes might become visible. However, we conclude their impact on OP density to be small.

Figure 9 shows the experimentally observed changes in bulk carrier recombination rates $\Delta R_{B,j}$ calculated using Equation (18) as well as the values $\Delta R_{B,\text{SRH},j}$ predicted by the model (see Equation (15)) for material pCz-high[TD]-1 using the parameters

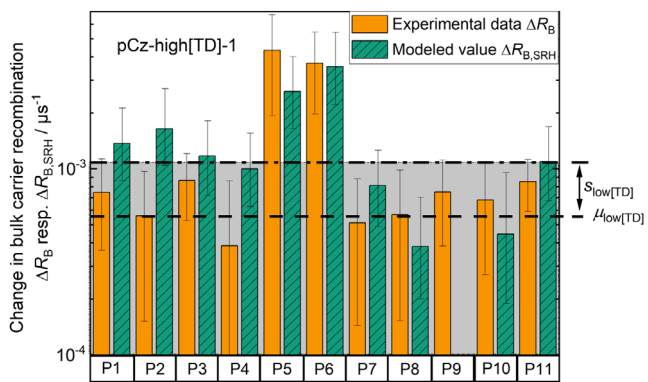


Figure 9. Experimental and modeled changes in bulk recombination ($\Delta R_{B,j}$ and $\Delta R_{B,\text{SRH},j}$, respectively) due to OP formation of all processes performed in the nucleation experiment for material pCz-high[TD]-1 after thermal oxidation process Ox1 (see Table 3). The error bars of the $\Delta R_{B,\text{SRH},j}$ values correspond to the uncertainties in C_0 (see Table 2). The mean value $\mu_{\text{low[TD]}}$ and standard deviation $s_{\text{low[TD]}}$ of all “low[TD]” materials of nucleation and growth experiments are indicated by dashed and dashed-dotted lines, respectively, and additionally by a grey background.

$Z = 0.02$ and $\gamma = 2.1$ from the calibration (cf., Figure 7). The error bars of the $\Delta R_{B,\text{SRH},j}$ values correspond to the uncertainty in C_0 (see Table 2), which is the largest uncertainty of the input parameters of the model. The minimum and maximum values of the error bars are calculated using $(C_0 - \Delta C_0)$ and $(C_0 + \Delta C_0)$ as input data for the interstitial oxygen concentration, respectively. The length of the green bar corresponds to the mean C_0 . Furthermore, the average value $\mu_{\text{low[TD]}}$ and the standard deviation $s_{\text{low[TD]}}$ of the experimental data $\Delta R_{B,j}$ for all “low[TD]” materials of experiments nucleation and growth are shown as well. Due to low C_{TD} (cf., Table 2), the “low[TD]” materials are expected not to exhibit significant oxygen precipitation. In these materials, thus, a negligible percentage of $\Delta R_{B,j}$ originated from OPs. This is consistent with the PL measurements presented in Figure 8 as well as with the predicted values from the model for the “low[TD]” materials of $\Delta R_{B,\text{SRH},j} < 3 \times 10^{-7} \mu\text{s}^{-1}$. Nevertheless, an increased change in bulk recombination rate can be found for the “low[TD]” materials due to the HT processes, which is $\Delta R_{B,j} = (5.5 \pm 5) \times 10^{-4} \mu\text{s}^{-1}$. We attribute this background recombination to other influences on bulk recombination, such as contaminations, which are further intensified during drive-in, or handling defects. Therefore, fine lined circular defect patterns, visible in PL, vanish in background recombination. As evidenced by Figure 9, for pCz-high[TD]-1, the experimentally observed $\Delta R_{B,j}$ of all processes except P5 and P6 are below the upper standard deviation of the background recombination.

The above-discussed relations regarding T_{dep} and duration within the nucleation temperature range are also visible in both experimental $\Delta R_{B,j}$ and modeled $\Delta R_{B,\text{SRH},j}$ values. However, the error bars for the experimental $\Delta R_{B,j}$ partly overlap. Due to differences in t_{dep} and T_{dep} , the model yields a lower $\Delta R_{B,\text{SRH}}$ value for process P4 than for P1. In contrast, P5 and P6 lead to the highest values, which agrees well with the experimental results for these two processes. Furthermore, process P8 results in a lower value

of the expected change in bulk carrier recombination $\Delta R_{B,\text{SRH}}$ than P10, which used a lower a_{dep} .

Beside these observations, the model predicts a lower $\Delta R_{B,\text{SRH}}$ for process P1 than for P2, which is attributed to the higher process starting temperature T_{start} at about 750 °C for P2 (cf., Table 3). This is the peak nucleation temperature, where the temperature fluctuates until it stabilizes during process start. Although a detectable recombination activity for P1 and P2 would be expected from the model, the experimental data show values around the background signal, leading to an inaccurate prediction of the model at this point. Furthermore, a lower $\Delta R_{B,\text{SRH}}$ is predicted for P3 compared to P1 and also for P7 than for P4, which can both be attributed to a steeper a_{drive} enhancing dissolution. This enhanced dissolution can also explain the lower $\Delta R_{B,\text{SRH}}$ for process P11 compared to P3, which is due to higher T_{drive} . For process P9, the model predicts a low change in bulk carrier recombination of $\Delta R_{B,\text{SRH},P9} = 2.1 \times 10^{-5} \mu\text{s}^{-1}$, which can be attributed to the time-lag in nucleation due to the 30 K decrease from deposition to drive-in plateau, as stated above. To infer any stronger conclusions from processes P3, P4 and P7 to P11 seems unjustified except that both experimental and predicted values agree with each other within their respective uncertainties and lie at the level of the background recombination.

For material nCz-high[TD]-1, all experimental $\Delta R_{B,j}$ values of the nucleation experiment are within the range of the background recombination of the “low[TD]” materials, although fine-lined circular defect patterns are visible in individually scaled PL images (cf., Figure 8) and the estimated average C_0 is higher than for pCz-high[TD]-1. This can be explained by the large uncertainty of $\Delta C_0 = 2.6 \times 10^{17} \text{ cm}^{-3}$ (cf., Table 2) resulting from the fit of C_{TD} versus C_0 .

4.2. Growth of Oxygen Precipitates

In Figure 10, individually scaled PL measurements are shown for material pCz-high[TD]-1 after processes P1 + Ox1, P12, P13 (shown for both, growth and dissolution experiments), P14, and P15. These processes were performed in three different experiments (cf., Table 2) and are therefore passivated using different techniques (see Section 3). The five processes share

an identical process start temperature T_{start} , deposition sequence (T_{dep} and t_{dep}), and slope of the temperature ramp up to drive-in plateau a_{drive} . Hence, according to the findings of Section 4.1, a similar OP density distribution can be assumed, when a possibly higher dissolution due to higher T_{drive} for processes P14 and P15 is neglected. Therefore, the only differences expected among the individual HT processes are OP size and, more precisely, surface area, leading to different changes in bulk recombination rate ΔR_B . The experimentally observed $\Delta R_{B,j}$ values calculated according to Equation (18) are tabulated below the PL measurements (see Figure 10).

In Figure 10, the $L_{\text{O}_i,j}$ values of the processes calculated according to Equation (20) are listed as well. Clearly, ΔR_B as well as the strength of the circular defect pattern in PL increases with L_{O_i} . Furthermore, we found an inverse correlation of the interstitial oxygen concentration C_0 with L_{O_i} for both “high[TD]” materials, while for both “low[TD]” materials no significant change was observed. For example, the difference in interstitial oxygen concentration measured after reference process P0 and process P15 was $\Delta C_0 = 8 \times 10^{16} \text{ cm}^{-3}$ for material pCz-high[TD]-1 and $\Delta C_0 = 2.4 \times 10^{17} \text{ cm}^{-3}$ for material nCz-high[TD]-2. Also, a correlation of the etch-pit density after Secco etch with L_{O_i} was found for the “high[TD]” materials, while for the “low[TD]” materials no impact was observed. For “high[TD]” materials, an increase in etch-pit density up to two orders of magnitude was found. Therefore, we conclude L_{O_i} to correlate with OP growth. Further details regarding the measurement procedures and results of etch-pit density and ΔC_0 determination have been reported in our previous studies.^[41,55]

For process P13, Figure 10 depicts PL measurements of a representative sample processed according to the dissolution (Diss) and growth (Growth) experiments. Although in both experiments neighboring wafers of the same ingot were processed using the same HT process, the results differ drastically. The samples processed in the dissolution experiment show slight circular defect pattern and $\Delta R_{B,P13,\text{Diss}} = 1.7 \times 10^{-3} \mu\text{s}^{-1}$, while for those processed in the growth experiment a very low PL signal was observed over almost the entire sample area (black area in PL), with $\Delta R_{B,P13,\text{Growth}} = 7.5 \times 10^{-2} \mu\text{s}^{-1}$. In contrast to all other samples processed in the growth experiment, the wet chemical processes prior to POCl_3 diffusion (saw damage etching and HCl

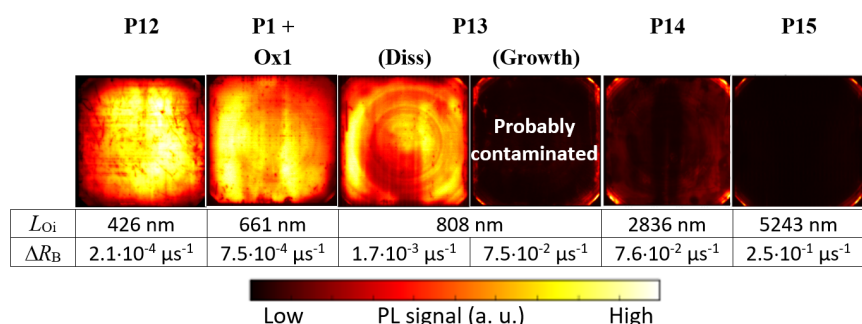


Figure 10. Individually scaled PL images of one representative symmetrical carrier lifetime sample of material pCz-high[TD]-1, processed using selected HT process variations differing only in t_{drive} and T_{drive} , and hence in L_{O_i} (neglecting a possible higher dissolution due to higher T_{drive}). For process P13 samples, processed according to the dissolution (Diss) and growth (Growth) experiments, are shown. Furthermore, the $L_{\text{O}_i,j}$ values (calculated using Equation (20)) as well as experimental $\Delta R_{B,j}$ values (calculated using Equation (18)) are tabulated. For the sample P13 of the dissolution experiment, ΔR_B is calculated using $\tau_{\text{eff},\text{P0}}$ of the nucleation experiment, whereas for the other variations $\tau_{\text{eff},\text{P0}}$ of the respective experiment is used.

treatment) of the samples for processes P13 and P17 were performed on a later day. Due to this “old” chemistry, these samples could exhibit a higher concentration of metallic impurities. As OPs are well known for gettering, we surmise that the OPs after POCl_3 diffusion are decorated with these impurities. This would increase the recombination activity of the OPs. For this reason, the results of processes P13 and P17 of the growth experiment are left out of consideration from further interpretation.

In **Figure 11**, the experimental $\Delta R_{B,j}$ values are shown for all investigated “high[TD]” materials versus the corresponding modeled changes in bulk recombination rates $\Delta R_{B,\text{SRH},j}$, using the parameters $Z = 0.02$ and $\gamma = 2.1$ inferred from calibration. The error bars of the $\Delta R_{B,\text{SRH},j}$ values correspond to the uncertainty in C_0 (see Table 2). It is noteworthy that the model calibration included the experimental data only of material pCz-high[TD]-1. The figure includes the results of all processes of the nucleation experiment with subsequent oxidation process, all processes of the growth experiment (except processes P13 and P17), and processes P13 and P20 of the dissolution experiment (see Table 3). Furthermore, the average value $\mu_{\text{low[TD]}}$ and standard deviation $s_{\text{low[TD]}}$ of the background recombination of the “low[TD]” materials are depicted analogous to Figure 9. In addition, the straight with slope 1 serving as a guide to the eye is the

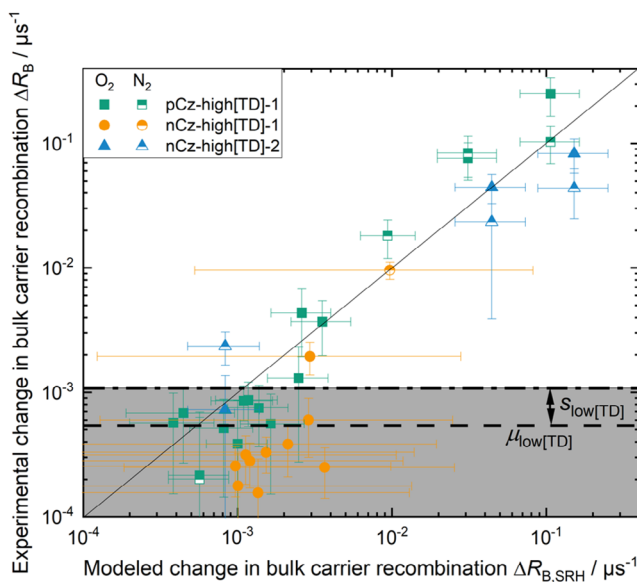


Figure 11. Experimental and modeled changes in bulk recombination rate ($\Delta R_{B,j}$ and $\Delta R_{B,\text{SRH},j}$, respectively) of all investigated “high[TD]” materials for all processes of the nucleation experiment with subsequent oxidation process, all processes of the growth experiment (except processes P13 and P17), and processes P13 and P20 of the dissolution experiment. The error bars of the $\Delta R_{B,\text{SRH},j}$ values correspond to the uncertainties in C_0 (see Table 2). For sample P13 and P20 of the dissolution experiment the experimental $\Delta R_{B,j}$ are calculated using $\tau_{\text{eff},\text{PO}}$ of the nucleation experiment, whereas for the other variations $\tau_{\text{eff},\text{PO}}$ of the respective experiment is used. The mean value $\mu_{\text{low[TD]}}$ and standard deviation $s_{\text{low[TD]}}$ of all “low[TD]” materials of nucleation and growth experiments are indicated by dashed and dashed-dotted lines, respectively, and additionally by a grey background. The straight line with slope 1 corresponds to a perfect match between model and experiment.

line on which data points would lie if experiment and model showed perfect agreement.

A good agreement is found between experiment and model over three orders of magnitude. Hence, a satisfactory description of the recombination due to the nucleation and growth of OPs in n-type as well as p-type silicon is achieved by the model in a range covering most HT processes relevant for photovoltaic applications.

Furthermore, within the experimental uncertainty, no influence of the gas atmosphere during drive-in can be identified when comparing identical material and HT temperature–time profiles performed in N_2 or O_2 ambient. Although this contrasts with literature statements,^[16,18,28] it may be explained by the growth of the PSG layer as a doping source at the very beginning of the investigated phosphorus diffusion, which takes place in an oxidizing ambient. Hence, the N_2 ambient applied thereafter, i.e., during drive-in, does not significantly enhance the nucleation rate and therefore only marginally affects oxygen precipitation. This finding was already reported in our previous work.^[41]

4.3. Dissolution of Oxygen Precipitates

As a third component for the description of oxygen precipitation, the dissolution is investigated using TR treatments. **Figure 12** shows PL measurements of all nine process variations of the dissolution experiment for materials pCz-high[TD]-1 and nCz-high[TD]-1. Without TR treatment (noTR), circular defect patterns are visible after processes P13 and P20 for both materials, whereas these patterns are more pronounced after process P20. In contrast, the reference groups, which are processed without any HT treatment, show no (pCz-high[TD]-1) or weak (nCz-high[TD]-1) defect patterns. Note in Figure 8 that no circular defect pattern appears in nCz-high[TD]-1 after processes P4 and P8. Therefore, the defect pattern visible without any thermal treatment can be attributed to the presence of TDs, which are annihilated due to a thermal treatment above 500 °C.^[2,16]

After both TR treatments (TR1000 and TR1050) without subsequent diffusion process, no circular defect pattern is found in material pCz-high[TD]-1, while material nCz-high[TD]-1 shows a weak pattern but on a high signal level in the wafer center. Despite a higher L_{OI} for the TR processes ($L_{\text{OI,TR1000}} = 1.8 \mu\text{m}$; $L_{\text{OI,TR1050}} = 2.8 \mu\text{m}$) and, hence, enhanced growth compared to processes P13 and P20 without previous TR process ($L_{\text{OI,P13}} = 0.8 \mu\text{m}$; $L_{\text{OI,P20}} = 1.3 \mu\text{m}$), weaker defect patterns are visible. This indicates that the OP density after the TR treatments must be lower than after processes P13 and P20. All wafers (“high[TD]” and “low[TD]”) that were subjected to a TR process show a low PL signal in the wafer corners, independent of subsequent POCl_3 diffusion processes. The origin of this low PL signal in the wafer corners is not yet understood. However, a relation to oxygen precipitation is unlikely because we observed this for both “high[TD]” and “low[TD]” materials.

Both samples subjected to a POCl_3 diffusion processes (P13 and P20) after the TR treatments exhibit circular defect patterns and a reduced PL signal. Similar to the samples processed without TR pretreatment (noTR), process P20 leads to a more severe defect pattern than process P13. This agrees with the difference in L_{OI} between processes P13 and P20 and hence the growth of

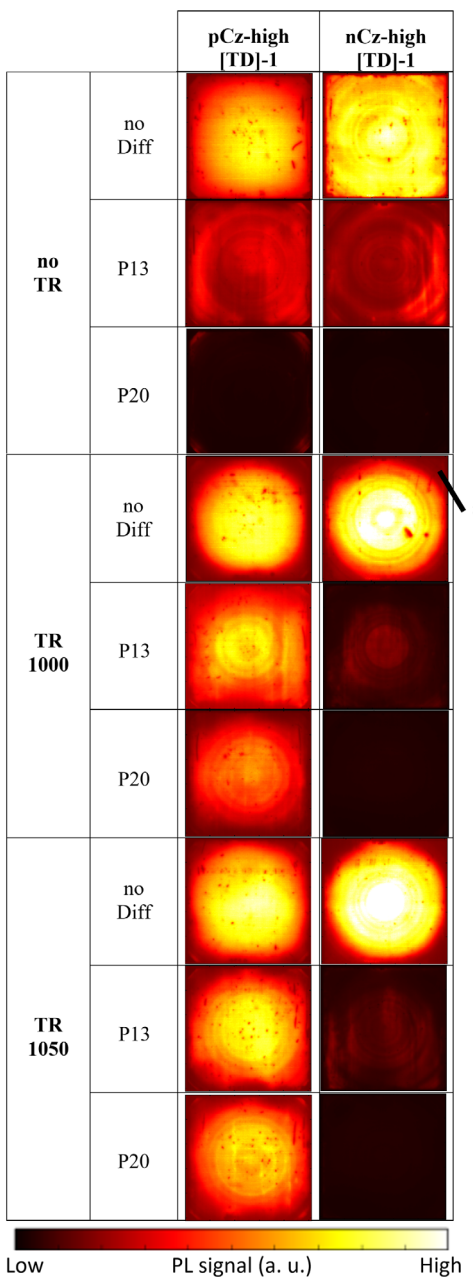


Figure 12. PL measurements of representative symmetrical carrier lifetime samples of materials pCz-high[TD]-1 and nCz-high[TD]-1 for all HT process combinations, performed in the dissolution experiment. Furthermore, the low PL signal in the wafer corners is indicated. All images refer to the same scale.

OPs. However, a major difference in the impact of the TR treatments can be found between pCz-high[TD]-1 and nCz-high[TD]-1 material. For material pCz-high[TD]-1, the defect pattern is weaker when a TR treatment has been performed prior to the POCl_3 diffusion process. This is evident by the comparison between processes P13 and P20 carried out in the versions noTR and with treatment TR1000. After pretreatment TR1050, the defect patterns are even weaker than after TR1000. In

contrast, the defect patterns are more distinct in material nCz-high[TD]-1 after a TR treatment prior to POCl_3 diffusion. This is evident for process P13, while for process P20 no difference is found due to the low PL signal of the samples processed with and without TR treatment. Due to the low signal intensity, a differentiation between TR1000 and TR1050 is not possible based on PL alone.

In **Figure 13**, the experimental $\Delta R_{B,j}$ values and modeled changes in bulk recombination rate $\Delta R_{B,\text{SRH},j}$ are shown for both “high[TD]” materials. The error bars of the $\Delta R_{B,\text{SRH},j}$ values are again derived from the uncertainty in C_0 (see Table 2). Due to lacking of a reference process P0 in the dissolution experiment as well as due to different “low[TD]” materials used in comparison with the nucleation and growth experiments, the calculation of the $\Delta R_{B,j}$ values for the “low[TD]” materials of the dissolution experiment is not possible. Instead, the background recombination of “low[TD]” materials of the nucleation and growth experiments is shown as in Figure 9 and 11. Note that for these samples the low PL signal in the wafer corners is not observed. For calculating $\Delta R_{B,j}$, the results of reference process P0, performed in the nucleation experiment, are used for both materials. Due to the low PL signal at the wafer corners, the TR processes were excluded from model calibration (see Section 4).

The $\Delta R_{B,j}$ values of the POCl_3 diffusion processes performed subsequent to a TR treatment show a major differences between materials pCz-high[TD]-1 and nCz-high[TD]-1, which is consistent with the PL images presented in Figure 12. While for material pCz-high[TD]-1 only process combination TR1000 + P20 exceeds the upper standard deviation of the “low[TD]” materials of experiments nucleation and growth, all process combinations including a TR treatment show significant $\Delta R_{B,j}$ values for material nCz-high[TD]-1. This difference between both “high[TD]” materials plausibly results from the difference in thermal donor concentration C_{TD} and hence in interstitial oxygen concentration

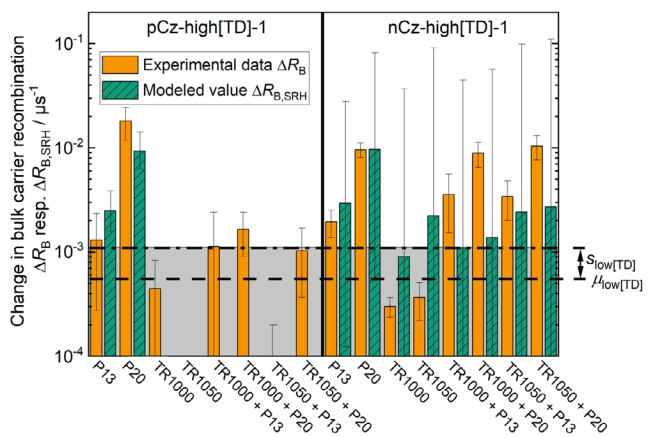


Figure 13. Experimental and modeled changes in bulk recombination ($\Delta R_{B,j}$ and $\Delta R_{B,\text{SRH},j}$, respectively) of all processes performed in the dissolution experiment for materials pCz-high[TD]-1 and nCz-high[TD]-1. The error bars of $\Delta R_{B,\text{SRH},j}$ correspond to the uncertainties in C_0 (see Table 2). The experimental $\Delta R_{B,j}$ are calculated using $\tau_{\text{eff},P0}$ of the nucleation experiment which does not feature a TR pretreatment. The mean value $\mu_{\text{low[TD]}}$ and standard deviation $s_{\text{low[TD]}}$ of all “low[TD]” materials of nucleation and growth experiments are indicated by dashed and dashed-dotted lines, respectively, and additionally a grey background.

C_0 in the as-cut state. Material nCz-high[TD]-1 exhibits $C_0 = (11.6 \pm 2.6) \times 10^{17} \text{ cm}^{-3}$ which is slightly higher than $C_0 = (9.5 \pm 0.4) \times 10^{17} \text{ cm}^{-3}$ for material pCz-high[TD]-1 (cf., Table 2). The higher of these values would lead to enhanced growth of nuclei formed in the temperature stabilization phase at about 745 °C at the very beginning of a TR treatment (cf., Table 3) and, hence, to a larger number of OPs surviving the subsequent temperature ramp up toward the TR temperature plateau. However, the difference in C_0 cannot be stated clearly because for material nCz-high[TD]-1 this value is derived from a fit of C_{TD} versus C_0 and is therefore accompanied by a significant error (cf., Table 2). Nevertheless, the difference in C_0 would furthermore explain the diverging impacts of the TR treatments. While for pCz-high[TD]-1 a higher TR temperature leads to a reduced OP density and, therefore, to a weaker defect pattern, this reduced OP density is compensated by a larger OP growth in material nCz-high[TD]-1 during TR1050, leading to similar A_{OP} . Consequently, we suggest a cutoff between an advantageous and disadvantageous impact of both performed TR treatments to lie in the range between the C_0 values of both “high[TD]” materials.

In the case of both materials and for processes P13 and P20 (noTR), ΔR_B and $\Delta R_{B,\text{SRH}}$ agree within the uncertainties of both values. For material pCz-high[TD]-1, the $\Delta R_{B,\text{SRH},j}$ values of all process combinations with a TR treatment prior to POCl_3 diffusion are below $10^{-4} \mu\text{s}^{-1}$. Here, the model predicts that almost no OPs should survive the TR treatment and the time-lag after the cool-down from the TR process prevents the formation of nuclei during the deposition phase of the subsequent diffusion process. In contrast, the PL images in Figure 12 show weak defect pattern after TR treatment followed by a POCl_3 diffusion. Furthermore, the experimental results in Figure 13 show a more pronounced impact of some process combinations, especially “TR1000 + P20”, where ΔR_B exceeds the upper standard deviation of the background recombination as mentioned above. A plausible explanation for the differences in $\Delta R_{B,j}$ and $\Delta R_{B,\text{SRH},j}$ is due to inadequate assumptions regarding the time-lag in nucleation, which is discussed in more detail in Section 5.

For nCz-high[TD]-1, an abrupt rise in ΔR_B is observed from both TR treatments toward subsequent POCl_3 diffusion processes. This is consistent with the PL images in Figure 12. One explanation for this could be the morphological transformation of OPs, and hence the start of enhanced recombination activity. This aspect is addressed in Section 5 in further detail.

The large uncertainty in C_0 of $\Delta C_0 = 2.6 \times 10^{17} \text{ cm}^{-3}$ for material nCz-high[TD]-1 (cf., Table 2) resulting from the fit of C_{TD} versus C_0 results in a strongly amplified uncertainty of $\Delta R_{B,\text{SRH},j}$, represented by the large uncertainty ranges in Figure 13. A quantitative comparison of $\Delta R_{B,\text{SRH}}$ with ΔR_B seems therefore difficult. Nevertheless, the model appears to be able to predict at least the trends in $\Delta R_{B,j}$ for all processes performed using material nCz-high[TD]-1.

4.4. Model Validation at the Level of PERCs

Figure 14 shows the energy conversion efficiencies of PERCs for all eight combinations of POCl_3 diffusion and thermal oxidation processes. Three peak temperatures of the contact firing process

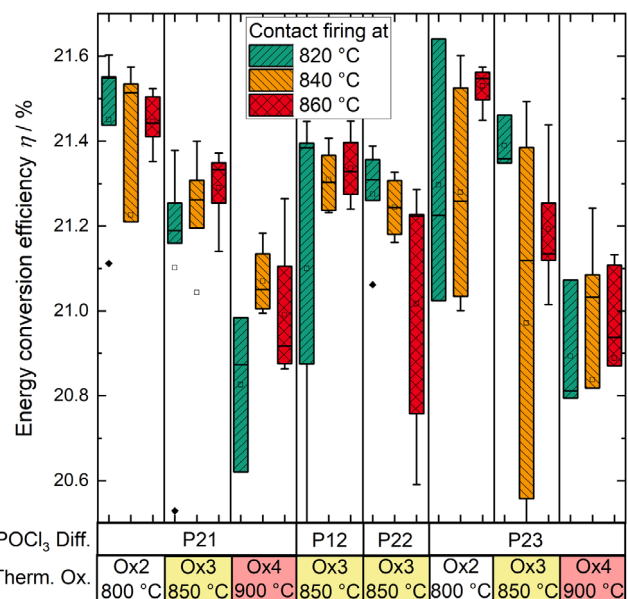


Figure 14. PERC energy conversion efficiencies η of all combinations of POCl_3 diffusion and thermal oxidation processes performed to validate the model. For each combination, three applied contact firing temperatures are investigated.

are applied for each combination in order to identify the optimum. For processes P21 and P23, where a variation of the thermal oxidation process has been performed, a decreased efficiency is observed with increasing oxidation temperature, irrespective of contact firing temperature.

The observed efficiency losses are based on both lower j_{SC} (not shown) and lower V_{OC} , which was previously reported to result from oxygen precipitation.^[1] Figure 15 shows the measured V_{OC} values for all investigated combinations and contact firing temperatures. The V_{OC} values follow the same trends as the cell efficiencies in Figure 14. Furthermore, the implied open-circuit voltage limit due to bulk recombination, $iV_{\text{OC,bulk}}$, derived from QSSPC measurements on back-etched and repassivated nonmetallized cell test structures, are shown as well. The $iV_{\text{OC,bulk}}$ values represent the impact of the bulk carrier recombination (neglecting surface recombination). It thus corresponds to the limitation of the V_{OC} of the solar cell by bulk recombination alone. The measured V_{OC} of the PERCs includes additional losses due to contact recombination and the finite dark saturation current density j_{oe} of the phosphorus-doped emitter, whose average $j_{\text{oe,av}}$ is also reported in Figure 15. Clearly, $iV_{\text{OC,bulk}}$ correlates with V_{OC} . For combination P23 + Ox2, $iV_{\text{OC,bulk}}$ is somewhat on the high side, which is explained by the comparatively high $j_{\text{oe,av}}$ of P23 + Ox2. This leads to a higher loss in V_{OC} obtained with this process. Therefore, we conclude that the observed trends in V_{OC} , and hence in efficiency, originate from limiting defects within the silicon bulk.

Figure 16 shows the measured effective charge carrier lifetime τ_{eff} for the back-etched and repassivated nonmetallized cell test structures for all HT process combinations. Furthermore, a PL measurement of an exemplarily sample is shown for each combination. These PL measurements are scaled individually to

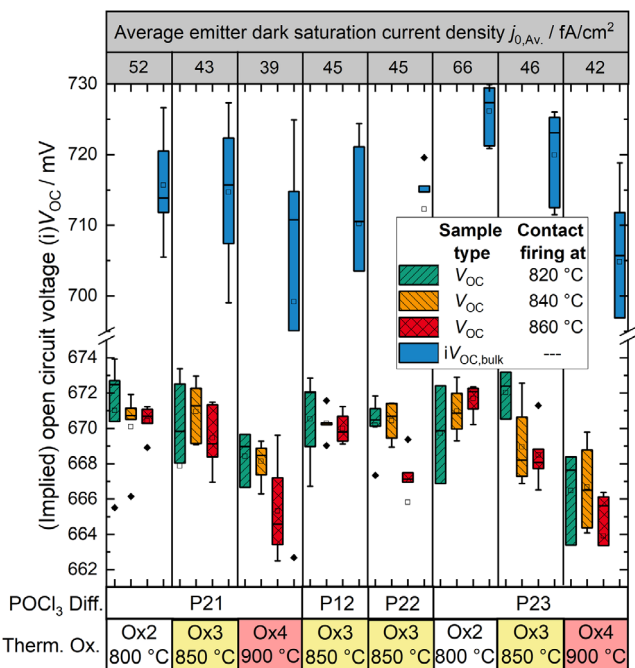


Figure 15. Open-circuit voltages V_{OC} of the PERCs for all combinations of POCl_3 diffusion and thermal oxidation processes performed to validate the model. For each combination, three applied contact firing temperatures are shown. Furthermore, the implied open-circuit voltages $iV_{OC,\text{bulk}}$ of carrier lifetime samples, achieved due to back-etch and passivation of the nonmetallized cell test structures, are shown for comparison. The average emitter dark saturation current densities of the emitters $j_{0e,\text{Avg}}$, measured on symmetrical samples (see Figure 6b), are listed at the top.

enhance the circular defect patterns. For groups showing these patterns, a reduced τ_{eff} is observed, which clearly shows oxygen precipitation to be the limiting factor for the bulk carrier lifetime.

The decrease in bulk carrier lifetime with increasing oxidation temperature agrees with higher L_{O_i} due to a higher oxidation temperature, indicating larger OP growth. The OP density is expected to remain constant for each individual POCl_3 diffusion process performed prior to oxidation. Processes P21 ($t_{\text{drive}} = 11 \text{ min}$), P12 ($t_{\text{drive}} = 17 \text{ min}$), and P22 ($t_{\text{drive}} = 23 \text{ min}$), all performed prior to a thermal oxidation process Ox3, show similar effective lifetimes. This suggests that the differences in L_{O_i} due to the variation of t_{drive} are less significant. Also, the comparison of combination P12 + Ox3 ($T_{\text{dep}} = 794 \text{ }^{\circ}\text{C}$) with P23 + Ox3 ($T_{\text{dep}} = 798 \text{ }^{\circ}\text{C}$) reveals similar effective lifetimes. This infers that the difference in T_{dep} of 4 K and hence in nucleation rate is also less significant.

Figure 16 also shows the modeled bulk carrier lifetime, where Auger recombination is considered using the SRH parametrization of Richter et al.^[60] in addition to OP-induced recombination from Equation (15). The error bars of the $\Delta R_{B,\text{SRH},j}$ values again correspond to the uncertainty in C_0 (see Table 2). The trends in the modeled results correlate with those of the experimental data. However, the model systematically underestimates τ_{eff} , which can be attributed to an overestimation of the mean C_0 .

As the silicon bulk material as well as the performed HT process variations in this experiment did not contribute to model

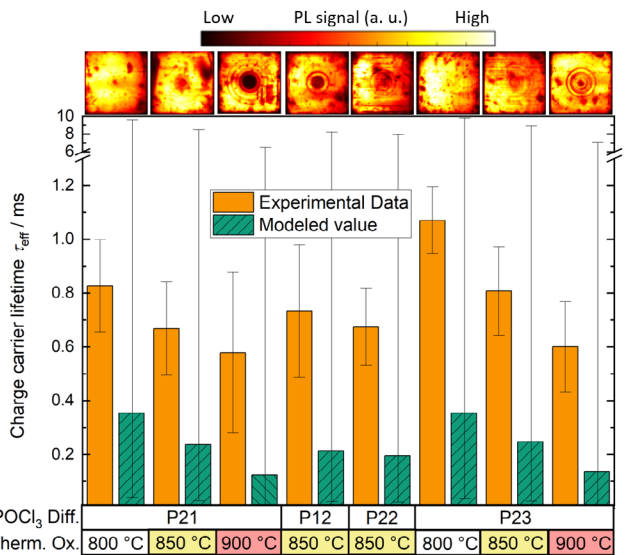


Figure 16. Measured and modeled effective charge carrier lifetime τ_{eff} at $\Delta n = 10^{15} \text{ cm}^{-3}$ of all combinations of POCl_3 diffusion and thermal oxidation processes. Experimental data were measured after etch back and repassivation of nonmetallized cell test structures. For modeling, Auger recombination is included according to Richter et al.^[59] in addition to OP-induced recombination from Equation (15). The error bars of the $\Delta R_{B,\text{SRH},j}$ values correspond to the uncertainty in C_0 (see Table 2) resulting from a fit of C_{TD} versus C_0 . Furthermore, individually scaled PL measurements of an exemplarily sample for each process combination are shown.

calibration, the observed agreement in trends lends further support to the broad applicability of the model.

4.5. Comparison of the Model with Numerical Simulation

We now put the present model into the context of our previous numerical simulation.^[41] For this purpose, exemplary HT processes and combinations thereof are simulated using the setup and parameters described in ref. [41] and the resulting $\Delta R_{B,\text{SRH},\text{Sim},j}$ values are reported in Figure 17. Note that for the simulation calibration, a different data base was used compared to the model of this work. Experimental data and values derived using the present model are shown for comparison. The error bars of the $\Delta R_{B,\text{SRH},j}$ values again correspond to the uncertainty in C_0 (see Table 2). For the $\Delta R_{B,\text{SRH},\text{Sim},j}$ values no error bars are available, as the simulation is performed using the average C_0 only. Note that the simulation results have already partly been published in ref. [41]. We use the same recombination parameters as in ref. [41] to calculate $\Delta R_{B,\text{SRH},\text{Sim},j}$, and thus difference in modeling results are directly related with differences in precipitate size and density. The results of the investigated HT processes are grouped into the three experimental sections such as nucleation, growth, and dissolution. Furthermore, the background recombination of the “low[TD]” materials of the nucleation and growth experiments is shown like on Figure 9, 11, and 13.

For the process combinations within the nucleation experiment, the simulation results in nearly identical $\Delta R_{B,\text{SRH},\text{Sim},j}$ values. This does not satisfactorily reflect the experimental data,

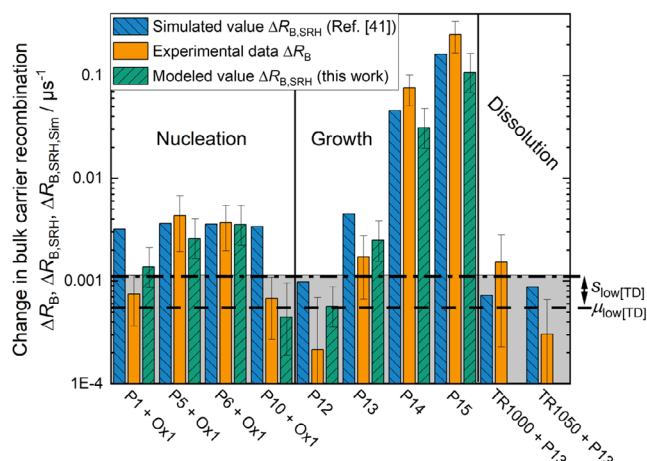


Figure 17. Simulated ($\Delta R_{B,\text{SRH,Sim},j}$, ref. [41]), experimental ($\Delta R_{B,j}$), and modeled ($\Delta R_{B,\text{SRH},j}$) changes in bulk recombination rate for exemplary HT processes and combinations thereof, grouped into nucleation, growth, and dissolution experiments. The mean value $\mu_{\text{low[TD]}}$ and standard deviation $s_{\text{low[TD]}}$ of all “low[TD]” materials of nucleation and growth experiments are indicated by dashed and dashed-dotted lines, respectively, and additionally by a grey background. For TR1000 + P13 and TR1050 + P13, the model yields $\Delta R_{B,\text{SRH},j}$ values below $10^{-4} \mu\text{s}^{-1}$.

which show lower ΔR_B within the background recombination for P1 + Ox1 and P10 + Ox1. Thus, the simulation overestimates nucleation for these process combinations, which results from an overestimation of nucleation during ingot cool-down where the time-lag in nucleation is not explicitly considered. The results of the present model show a closer agreement with the experimental data.

For the growth experiment, the differences between the processes are well captured by different L_{O} values, originating in different t_{drive} or T_{drive} values (cf., Table 3). Here, a good agreement with experimental data is found with both the simulation from ref. [41] and the model of this work. This is not the case for the process combinations within the dissolution experiment. For the derived model, this deviation might be explained by inadequate assumptions regarding the time-lag in nucleation, as already mentioned in Section 4.3, leading to $\Delta R_{B,\text{SRH},j}$ values below $10^{-4} \mu\text{s}^{-1}$.

Based on the different description of nucleation by the model of this work, an enhanced agreement with the experimental $\Delta R_{B,j}$ values is achieved. Note that in contrast with the parameters of simulation from ref. [41] the parameters of the model of this work were fitted with the help of the nucleation experiments. Nevertheless, some questions remain open. These regard, in particular, the time-lag in nucleation and the start of enhanced recombination activity. Corresponding answers may contribute to a further improvement of the model. These aspects are further discussed in Section 5.

5. Discussion

5.1. Time-lag in Nucleation

A key aspect in the description of oxygen precipitates in this work is the explicit implementation of a time-lag in nucleation, which

was determined for a steep temperature decrease ($>100 \text{ K h}^{-1}$) starting from an initial temperature above 900°C with a temperature reduction of at least $\Delta T = 100 \text{ K}$.^[22] Noteworthily, these specifications represent the lower bounds of the conditions investigated in ref. [22]. Therefore, on the basis of ref. [22], it cannot be excluded that a lower initial temperature or a lower ΔT may also cause a time-lag in nucleation.

When the time-lag in nucleation is neglected, the OP density after a HT process is dominated by the nuclei formed during the ingot cool-down. Without time-lag, for example, with a temperature drop from 1000 to 500°C during ingot cool-down with a slope of 100 K h^{-1} , 74% of A_{OP} would result from nucleation during this cool-down, while the deposition sequence of process P5 with subsequent thermal oxidation Ox1 (cf., Table 3) would only account for 26% of A_{OP} . Note that this process includes an extended deposition of $t_{\text{dep}} = 63 \text{ min}$ at $T_{\text{dep}} = 794^\circ\text{C}$. Therefore, in a scenario without time-lag, the nucleation during the deposition sequence of a POCl_3 diffusion process would have only a minor impact on A_{OP} and thus ΔR_B in general. This is in contradiction to the experimental results shown in Section 4.1, which show that the deposition sequence leads to a variation in ΔR_B by one order of magnitude, and hence has a major impact on the OP density. Furthermore, when allowing nucleation during ingot cool-down, we were unable to find model parameters yielding a consistent description of all experimental observations. As a consequence, we are drawn to conclude that nucleation during ingot cool-down is limited by nucleation time-lag as observed by Inoue et al.^[22]

On the other hand, a persistent time-lag in nucleation would also suppress the nucleation rate in the subsequent solar cell process, which does not agree with the experimental observations of Section 4.1. The experimental evidence therefore suggests that the time-lag is overcome by a dwell time of several hours at 450°C , as also observed by Inoue et al.^[22] This dwell time is given when the ingot cool-down temperature–time profile flattens out at low temperatures. The comparison of the model of this work with the simulation from ref. [41] presented in Section 4.5 demonstrates the high relevance of the time-lag. Indeed, the simulation from ref. [41] leads to nearly identical results of the processes performed in the nucleation experiment, in contrast with the experimental data. The occurrence of a time-lag in nucleation strongly depends on the cooling rate, as stated in ref. [22], and hence on the pulling rate of an ingot. This could explain the results of Korsós et al.,^[3] who found small BMDs after an ingot cool-down with a relatively low pulling rate of 36 mm h^{-1} (leading to the cooling rate of about 100 K h^{-1}), which grew during subsequent HT processing. In current Cz-Si manufacturing (especially for photovoltaics) the pulling rate is much higher ($\geq 60 \text{ mm h}^{-1}$),^[18,21] leading to cooling rates of $\gg 100 \text{ K h}^{-1}$ at high temperatures. In this case, a time-lag in nucleation is very likely.

An unknown aspect of the time-lag is the degree of reduction in nucleation rate J_0 . In this work, we assume a complete suppression of nucleation to $J_0 = 0 \text{ cm}^{-3} \text{ s}^{-1}$ during the time-lag. A finite J_0 could explain the observed circular defect pattern of material pCz-high[TD]-1 in the dissolution experiment after both TR treatments with subsequent POCl_3 diffusion process (cf., Figure 12). An only partially reduced nucleation during ingot cool-down could result in OPs with radii large enough to survive

TR treatments. In this case, higher temperatures corresponding to larger r_c values will reduce the density of surviving OPs. This would explain the weaker defect pattern after TR1050 compared with TR1000, both with subsequent POCl_3 diffusion. This minor nucleation during ingot cool-down would be significant for processes such as TR treatments resulting in a low density of OPs with a large size. For processes resulting in a high OP density and/or low OP size, which holds for all other processes presented in this work, an indication for a significant impact of a finite J_0 was neither found nor expected.

In any case, it is clear that the model proposed in this work requires the implementation of a time-lag, along the lines of Inoue et al.,^[22] in order to reproduce the experimental findings. As mentioned above, other publications^[39–41] considered the retardation in nucleation implicitly, due to very slow formation of oxygen-particles consisting of only several O atoms.

5.2. Start of Enhanced Recombination

The morphological transformation from unstrained to strained OPs has been concluded to be the starting point of enhanced recombination activity.^[33] This transformation has also been identified as the starting point of impurity gettering at the OPs,^[31] whereby gettered impurities enhance the effective defect density at the same trap levels associated with OPs.^[35] However, the mechanisms behind this transformation are not fully understood.^[31] Falster et al.^[31] derived an empirical model for the dwell time t_g at a given growth temperature necessary to transform an amount of 10^7 cm^{-3} unstrained OPs into strained ones. These authors took this density of strained OPs as the starting point of effective gettering and hence enhanced recombination activity. The transformation proceeds at a temperature-dependent rate within a population of growing OPs and does not depend on their size but on their density and on C_0 . These parameters represent the input data of the empirical model of ref. [31]. However, as that model is based on a constant growth temperature and a constant density of unstrained OPs, an adaption for HT processes with varying temperatures and continuous nucleation seems challenging. Therefore, a starting point of enhanced recombination has not been included in the present model and hence all OP-related oxygen aggregations (excluding embryos in the equilibrium state^[22]) are considered for the calculation of A_{OP} and assumed to similarly contribute to carrier recombination.

Nevertheless, important information can be derived from the empirical model of Falster et al.^[31] For given C_0 and density of unstrained OPs, t_g decreases with increasing temperature until a minimum at around 950°C is reached, whereafter t_g increases again. For example, at $C_0 = 10^{18} \text{ cm}^{-3}$ and a density of unstrained OPs of 10^{10} cm^{-3} , dwell times for the start of enhanced recombination at 860 and 950°C are calculated to be $t_{g,860} = 64 \text{ min}$ and $t_{g,950} = 19 \text{ min}$, respectively. At this C_0 , the ratio $t_{g,860}/t_{g,950}$ is 3.3 and is constant for all densities of unstrained OPs, whereas the absolute t_g values decrease with increasing density of unstrained OPs.

For material nCz-high[TD]-1 investigated in the dissolution experiment, C_0 was estimated to be close to 10^{18} cm^{-3} by a fit of C_{TD} versus C_0 (cf., Table 2). Furthermore, the two POCl_3 diffusion processes P13 and P20, performed after the TR

treatments, exhibit $T_{\text{drive},\text{P13}} = 860^\circ\text{C}$ and $T_{\text{drive},\text{P20}} = 950^\circ\text{C}$ as well as $t_{\text{drive},\text{P13}} = 125 \text{ min}$ and $t_{\text{drive},\text{P20}} = 35 \text{ min}$, respectively (cf., Table 3). This leads to $t_{\text{drive},\text{P13}}/t_{\text{drive},\text{P20}} = 3.6$, which is slightly higher than $t_{g,860}/t_{g,950} = 3.3$. Hence, when the transformation of 10^7 cm^{-3} unstrained OPs into strained ones is reached for process P20, the empirical model suggests the same to be also true for process P13. This could explain the abrupt rise in ΔR_B observed from both TR treatments toward subsequent POCl_3 diffusion processes (see Figure 13). Due to the low OP density resulting from TR treatment as well as the long t_g during TR treatment, the transformation of 10^7 cm^{-3} unstrained OPs is reached only during drive-in sequence of the subsequent POCl_3 diffusion processes.

However, we suggest this potential observation of the starting point of enhanced recombination activity to be due to the special character of the TR treatments, regarding density of unstrained OPs and t_g as discussed above. No other process presented in this work showed an indication for a weaker recombination activity of the OPs, although the model yields a OP density at the end of the processes in the range of 10^8 to $7 \times 10^{10} \text{ cm}^{-3}$ for all “high[TD]” materials. Therefore, we suspect the transformation of 10^7 cm^{-3} unstrained OPs to be completed until the end of these processes.

6. Conclusion

This work presented a model to predict the silicon bulk carrier lifetime limit due to oxygen precipitation during high temperature processes in photovoltaic applications. The model is easily implemented without resorting to specialized numerical simulation tools. The calculation is based on the temperature–time profile of high-temperature processes and the properties of the silicon bulk as the input data. In addition to published analytical descriptions of oxygen precipitation, an empirical description of the retarded growth of small precipitates is included with a parameter γ describing the strength of the retardation. The model features only two free parameters, namely, γ and the Zeldovich factor Z . A key aspect of the model is the explicit implementation of a time-lag in nucleation. This time-lag leads to negligible nucleation during ingot cool-down and thus to a more relevant nucleation during solar cell processing. In comparison to our previous simulation,^[41] this explicit implementation of the time-lag in combination with a larger data base for calibration yields a better description of OP nucleation during solar cell processing. This agreement extends to different silicon materials, which were not used to calibrate the model. Furthermore, the predictive power of the model is demonstrated by comparison with the efficiencies and bulk carrier lifetimes of PERCs. These cells were fabricated using a silicon material and high temperature processes that did not contribute to model calibration, indicating a broad predictive validity of the model. Note that the present model disregards cases where the time-lag in nucleation is overcome, which is reported to happen for HT sequences of more than 10 h or for processes at 450°C of several hours. In these cases, a deviation from model predictions is expected.

Questions regarding the degree of reduction in nucleation rate J_0 during time-lag remain open for the time being. This question is most important for processes leading to a reduced OP

density, e.g., TR treatments, where a minor number of OPs present after ingot cool-down can grow to a significant size. Furthermore, a change in recombination activity due to a morphological transformation of the OPs can get observable for these processes, which would also lead to a deviation from the prediction of the model. Possible effects of impurities, other than oxygen, involved in OP formation, as known for carbon, antimony, nitrogen, and hydrogen,^[16] might cause further deviations.

Despite these open questions, the proposed model satisfactorily describes the main trends of OP-related changes in bulk carrier recombination for a variety of silicon materials and HT processes. It therefore potentially helps to reduce process development costs and to ensure process stability with respect to material property variations.

As a final comment, the analytical approach of this model might also be used to describe other diffusion-limited phenomena of spherical precipitation in silicon, such as the precipitation of inactive phosphorus or of metallic impurities.

Acknowledgements

This work was funded by the German Federal Ministry for Economic Affairs and Energy BMWi in projects "POLDI" (contract number 0324079D) and "GENESIS" (contract number 0324274C). The authors would like to thank the research teams at Fraunhofer ISE PV-TEC, especially S. Schmidt and U. Belledin for the technical support with the thermal processes as well as S. Lohmüller for fruitful discussions.

Open Access funding enabled and organized by Projekt DEAL.

Conflict of Interest

The authors declare no conflict of interest.

Data Availability Statement

The data that support the findings of this study are available from the corresponding author upon reasonable request.

Keywords

bulk lifetime, Czochralski, modeling, oxygen precipitate, recombination

Received: October 28, 2022

Revised: December 1, 2022

Published online: December 25, 2022

- [1] L. Chen, X. Yu, P. Chen, P. Wang, X. Gu, J. Lu, D. Yang, *Sol. Energy Mater. Sol. Cells* **2011**, *95*, 3148.
- [2] J. Haunschild, J. Broisch, I. Reis, S. Rein, *Photovolt. Int.* **2012**, *15*, 40.
- [3] F. Korsós, L. Roszol, F. Jay, J. Veirman, A. D. Draoua, M. Albaric, T. Szarvas, Z. Kiss, A. Szabó, I. Soczó, G. Nádudvari, N. Laurent, *Sol. Energy Mater. Sol. Cells* **2018**, *186*, 217.
- [4] Y. C. Wang, in *nPV Workshop*, Hamelin, Conexio-PSE GmbH, Freiburg, Germany **2021**.
- [5] O. Nielsen, in *nPV Workshop*, Hamelin, Conexio-PSE GmbH, Freiburg, Germany **2021**.
- [6] *Inter. Technology Roadmap for Photovoltaic (ITRPV): 2021 Results*, Verband deutscher Maschinen- und Anlagenbau (VDMA), Frankfurt, Germany **2022**.
- [7] F. Feldmann, M. Bivour, C. Reichel, M. Hermle, S. W. Glunz, presented at *28th European PV Solar Energy Conf. and Exhibition*, WIP Wirtschaft und Infrastruktur GmbH und Co Planungs KG, München, Germany, Paris, France, September–October, **2013**.
- [8] F. Feldmann, M. Bivour, C. Reichel, H. Steinkeper, M. Hermle, S. W. Glunz, *Sol. Energy Mater. Sol. Cells* **2014**, *131*, 46.
- [9] R. Preu, E. Lohmüller, S. Lohmüller, P. Saint-Cast, J. M. Greulich, *Appl. Phys. Rev.* **2020**, *7*, 41315.
- [10] S. A. McHugo, E. R. Weber, S. M. Myers, G. A. Petersen, *J. Electrochem. Soc.* **1998**, *145*, 1400.
- [11] H. Hieslmair, A. A. Istratov, S. A. McHugo, C. Flink, T. Heiser, E. R. Weber, *Appl. Phys. Lett.* **1998**, *72*, 1460.
- [12] T. Y. Tan, E. E. Gardner, W. K. Tice, *Appl. Phys. Lett.* **1977**, *30*, 175.
- [13] R. J. Falster, M. Cornara, D. Gambaro, M. Olmo, M. Pagani, *SSP* **1997**, *57*–58, 123.
- [14] W. B. Henley, L. Jastrzebski, N. F. Haddad, *MRS Proc.* **1992**, *262*, 993.
- [15] W. C. McColgin, J. P. Lavine, C. V. Stancampiano, *MRS Proc.* **1995**, *378*, <https://doi.org/10.1557/PROC-378-713>.
- [16] A. Borghesi, B. Pivac, A. Sassella, A. Stella, *J. Appl. Phys.* **1995**, *77*, 4169.
- [17] R. C. Newman, *J. Phys. Condens. Matter* **2000**, *12*, R335.
- [18] D.-H. Hwang, S.-M. Hur, K.-H. Lee, *J. Cryst. Growth* **2003**, *249*, 37.
- [19] J. Veirman, B. Martel, E. Letty, R. Peyronnet, G. Raymond, M. Cascant, N. Enjalbert, A. Danel, T. Desrues, S. Dubois, C. Picoulet, X. Brun, P. Bonnard, *Sol. Energy Mater. Sol. Cells* **2016**, *158*, 55.
- [20] P. Hopfgartner, P. Collareta, M. Porrini, *Mater. Sci. Eng. B Solid.* **2000**, *73*, 158.
- [21] H. Nakanishi, H. Kohda, K. Hoshikawa, *J. Cryst. Growth* **1983**, *61*, 80.
- [22] N. Inoue, K. Watanabe, K. Wada, J. Osaka, *J. Cryst. Growth* **1987**, *84*, 21.
- [23] M. Tomassini, J. Veirman, R. Varache, E. Letty, S. Dubois, Y. Hu, O. Nielsen, *J. Appl. Phys.* **2016**, *119*, 84508.
- [24] E. Olsen, T. Mehl, H. E. Stalheim, M. Juel, R. Søndenå, I. Burud, *Phys. Status. Solidi A* **2022**, *219*, 2100655.
- [25] F. Schindler, M. C. Schubert, A. Kimmerle, J. Broisch, S. Rein, W. Kwapił, W. Warta, *Sol. Energy Mater. Sol. Cells* **2012**, *106*, 31.
- [26] F. Schindler, M. Forster, J. Broisch, J. Schön, J. Giesecke, S. Rein, W. Warta, M. C. Schubert, *Sol. Energy Mater. Sol. Cells* **2014**, *131*, 92.
- [27] T. Niewelt, S. Lim, J. Holtkamp, J. Schön, W. Warta, D. Macdonald, M. C. Schubert, *Sol. Energy Mater. Sol. Cells* **2014**, *131*, 117.
- [28] W. von Ammon, A. Sattler, G. Kissinger, in *Springer Handbooks, Springer Handbook of Electronic and Photonic Materials* (Eds: S. Kasap, P. Capper), Springer International Publishing, Cham **2017**, p. 1.
- [29] V. LaSalvia, A. Youssef, M. A. Jensen, E. E. Looney, W. Nemeth, M. Page, W. Nam, T. Buonassis, P. Stradins, *Prog. Photovolt. Res. Appl.* **2018**, *70*, 1572.
- [30] D. C. Walter, B. Lim, R. Falster, J. Binns, J. Schmidt, D. Walter, in *28th EU PVSEC*, WIP Wirtschaft und Infrastruktur GmbH und Co Planungs KG, München, Germany **2013**, pp. 699–702.
- [31] R. J. Falster, V. V. Voronkov, V. Y. Resnick, M. G. Mil'vidskii, *SSP* **2005**, *108*–109, 97.
- [32] K. S. Choe, *J. Electrochem. Soc.* **1995**, *142*, 1647.
- [33] J. D. Murphy, K. Bothe, M. Olmo, V. V. Voronkov, R. J. Falster, *J. Appl. Phys.* **2011**, *110*, 53713.
- [34] J. D. Murphy, M. Al-Amin, K. Bothe, M. Olmo, V. V. Voronkov, R. J. Falster, *J. Appl. Phys.* **2015**, *118*, 215706.
- [35] J. D. Murphy, R. E. McGuire, K. Bothe, V. V. Voronkov, R. J. Falster, *Sol. Energy Mater. Sol. Cells* **2014**, *120*, 402.
- [36] R. Basnet, C. Sun, H. Wu, H. T. Nguyen, F. E. Rougier, D. Macdonald, *J. Appl. Phys.* **2018**, *124*, 243101.
- [37] A. Le Donne, S. Binetti, V. Folegatti, G. Coletti, *Appl. Phys. Lett.* **2016**, *109*, 033907.

- [38] J. Schön, A. Youssef, S. Park, L. E. Mundt, T. Niewelt, S. Mack, K. Nakajima, K. Morishita, R. Murai, M. A. Jensen, T. Buonassisi, M. C. Schubert, *J. Appl. Phys.* **2016**, *120*, 105703.
- [39] R. Basnet, H. Sio, M. Siriwardhana, F. E. Rougieux, D. Macdonald, *Phys. Status. Solidi A* **2021**, *218*, 2000587.
- [40] B. C. Trzynadlowski, S. T. Dunham, *J. Appl. Phys.* **2013**, *114*, 243508.
- [41] J. Schon, T. Niewelt, D. Mu, S. Maus, A. Wolf, J. D. Murphy, M. C. Schubert, *IEEE J. Photovolt.* **2021**, *11*, 289.
- [42] Oxygen, Carbon, Hydrogen, and Nitrogen in Crystalline Silicon: Symp. Held December 2–5, 1985, Boston, Massachusetts, U.S.A (Eds: J. C. Mikkelsen, S. J. Pearton, J. W. Corbett, S. J. Pennycook), Materials Research Society, Pittsburgh, PA **1986**.
- [43] S. P. Fisenko, G. Wilemski, *Phys. Rev. E: Stat., Nonlinear, Soft Matter* **2004**, *70*, 56119.
- [44] F. S. Ham, *J. Phys. Chem. Solids* **1958**, *6*, 335.
- [45] N. Inoue, K. Wada, J. Osaka, *J. Electrochem. Soc.* **1981**, *128*, 282.
- [46] W. Shockley, W. T. Read, *Phys. Rev.* **1952**, *87*, 835.
- [47] J. Schmidt, D. Macdonald, *J. Appl. Phys.* **2005**, *97*, 113712.
- [48] M. A. Green, *J. Appl. Phys.* **1990**, *67*, 2944.
- [49] T. Niewelt, M. Selinger, N. E. Grant, W. Kwapis, J. D. Murphy, M. C. Schubert, *J. Appl. Phys.* **2017**, *121*, 185702.
- [50] U. Varshney, B. Hallam, P. Hamer, A. Ciesla, D. Chen, S. Liu, C. Sen, A. Samadi, M. Abbott, C. Chan, B. Hoex, *IEEE J. Photovolt.* **2019**, *10*, 19.
- [51] S. Werner, S. Mourad, W. Hasan, A. Wolf, *Energy Proc.* **2017**, *124*, 455.
- [52] A. Bentzen, A. Holt, *Mater. Sci. Eng. B Solid.* **2009**, *159–160*, 228.
- [53] J. Schön, V. Vähäniemi, A. Haarahiltunen, M. C. Schubert, W. Warta, H. Savin, *J. Appl. Phys.* **2014**, *116*, 244503.
- [54] A. Peral, A. Dastgheib-Shirazi, H. Wagner, G. Hahn, C. del Cañizo, *Energy Proc.* **2015**, *77*, 311.
- [55] M. B. Shabani, T. Yamashita, E. Morita, *SSP* **2007**, *131–133*, 399.
- [56] S. Maus, S. Lohmüller, D. Mu, J. Schön, T. Niewelt, A. Wolf, R. Preu, presented at *36th European PV Solar Energy Conf. and Exhibition*, Marseille, France, September 2019.
- [57] S. Werner, E. Lohmüller, P. Saint-Cast, J. M. Greulich, J. Weber, S. Schmidt, A. Moldovan, A. A. Brand, T. Dannenberg, S. Mack, S. Wasmer, M. Demant, M. Linse, R. Ackermann, A. Wolf, R. Preu, presented at *33rd European PV Solar Energy Conf. and Exhibition*, Amsterdam, The Netherlands, September **2017**.
- [58] D. E. Kane, R. M. Swanson, in *18th IEEE Photovoltaic Specialists Conf.* **1985**, pp. 578–583.
- [59] A. Kimmerle, J. Greulich, A. Wolf, *Sol. Energy Mater. Sol. Cells* **2015**, *142*, 116.
- [60] A. Richter, S. W. Glunz, F. Werner, J. Schmidt, A. Cuevas, *Phys. Rev. B* **2012**, *86*.
- [61] F. Mosei, A. Mochanov, B. Fischer, D. Krischel, A. Seidl, B. Birkmann, in *27th EU PVSEC*, WIP Wirtschaft und Infrastruktur GmbH und Co Planungs KG, München, Germany **2012**, pp. 933–938.